

Burnt-Net: Wildfire burned area mapping with single post-fire Sentinel-2 data and deep learning morphological neural network



Seyd Teymoor Seydi ^{a,1}, Mahdi Hasanlou ^{a,2,*}, Jocelyn Chanussot ^{b,c,3}

^a School of Surveying and Geospatial Engineering, College of Engineering, University of Tehran, Tehran, Iran

^b Aerospace Information Research Institute, Chinese Academy of Sciences, Beijing, PR China

^c Université Grenoble Alpes, CNRS, Grenoble INP, GIPSA-Lab, 38000 Grenoble, France

ARTICLE INFO

Keywords:

Deep learning
Semantic segmentation
Burned area
Sentinel-2
Morphological operator

ABSTRACT

Accurate and timely mapping of wildfire burned areas is crucial for post-fire management, planning, and next subsequent actions. The monitoring and mapping of the burned area by traditional and common methods are time-consuming and challenging while is vital to propose an advanced burned area detection framework for achieving reliable results. To this end, this study proposed a novel End-to-End framework based on deep learning and post-fire Sentinel-2 imagery. The proposed framework known as *Burnt-Net* combines quadratic morphological operators and standard convolution layers. The multi-patch multi-level residual morphological (MP-MRM) blocks are the main part of the decoder part of the *Burnt-Net* while the encoder part uses the multi-level residual morphological and transpose convolution layers. To evaluate the efficiency of *Burnt-Net* the post-fire Sentinel-2 for the latest wildfires over different countries was collected and then, the model was trained and evaluated based on them. Furthermore, the most common deep learning-based model implemented for comparing the result of burned areas by the proposed *Burnt-Net*. The results of burned areas mapping show the *Burnt-Net* is robust in the detection of burned areas and provides a mean accuracy of more than 97% by overall accuracy (OA). Furthermore, the *Burnt-Net* is fast and can provide the burned area map in the near real-time.

1. Introduction

Today, wildfires are known as one of the most important factors, which threaten the environment. Every year, a high amount of forest and other areas have been burned by wildfires in the whole of the world (Cardil et al., 2021; Wang et al., 2021). Wildfires affect many factors on our planet such as the emission of black carbon, negative effects on soil, wildlife threat, an increase in potential landslides, and old-growth forest losses (Pinto et al., 2022; Radocaj et al., 2022). Therefore, on-time and accurate knowledge of the extent of the burned areas (BA) is crucial for subsequent actions. The result of burned area mapping has many important applications including fire prediction (Michael et al., 2021), burnt biomass estimation (Shiraishi and Hirata, 2021), and mapping of high potential fire areas (Naderpour et al., 2021).

Satellite imagery provides the most valuable information about the Earth with minimum cost and time on a global scale. With the coming

new series of satellite imagery (i.e. Landsat-9, Sentinel-2) in addition to improving data quality, the temporal resolution of the dataset has been significantly improved (McCorkel et al., 2018). Accordingly, the use of remote sensing has been considered in many applications such as classification (Ahmad et al., 2021; Sellami and Tabbone, 2022), active fire monitoring (Wang et al., 2022; Xu et al., 2021b), flood mapping (Lupichini et al., 2022; Muñoz et al., 2021), and damage mapping (ElGharbawi and Zarzoura, 2021; Pilger et al., 2020).

Due to the increase in the availability of remote sensing datasets, wildfires have received significant attention in past years (Morresi et al., 2022; Smith-Ramírez et al., 2022). In this regard, the many researches have been done for burned area mapping based on medium resolution optical datasets (Campagnolo et al., 2021), synthetic aperture radar images (Zhang et al., 2021b), high-resolution datasets (Gajardo et al., 2022), and very high resolution (VHR) datasets (Warner et al., 2017). Furthermore, many burned area products have been provided based on

* Corresponding author.

E-mail addresses: seydi.teymoor@ut.ac.ir (S.T. Seydi), hasanlou@ut.ac.ir (M. Hasanlou), jocelyn.chanussot@grenoble-inp.fr (J. Chanussot).

¹ 0000-0002-3678-4877.

² 0000-0002-7254-4475.

³ 0000-0003-4817-2875.

<https://doi.org/10.1016/j.ecolind.2022.108999>

Received 21 April 2022; Received in revised form 16 May 2022; Accepted 17 May 2022

Available online 23 May 2022

1470-160X/© 2022 The Authors. Published by Elsevier Ltd. This is an open access article under the CC BY-NC-ND license (<http://creativecommons.org/licenses/by-nc-nd/4.0/>).

high and medium resolution datasets on the local and global scale (Chuvieco et al., 2016; Franquesa et al., 2022; Hawbaker et al., 2020; Otón et al., 2021b). The accuracy of the Moderate Resolution Imaging Spectroradiometer (MODIS) burned area product has been reported by some researches (Boschetti et al., 2016; Otón et al., 2021a; Vetrata et al., 2021). For example, Boschetti et al. (2019) reported the globally MCD64A1 product had an estimated *Commission* and *Omission* Errors of 40.2% and 72.6%, respectively. Moreover, the results of the accuracy assessment for MODIS burned area products are different and deepened on characteristics of region-of-interest. However, the medium resolution sensors have a high temporal resolution but mapping burned areas in more detail and high accuracy needs a fine spatial resolution dataset and advanced methods.

In past years, many burned area mapping methods have been developed based on the high-resolution dataset (Barboza Castillo et al., 2020; Farasin et al., 2020; Knopp et al., 2020). Mainly, these methods focused on change detection based on manual feature generation. These methods can be applied in two main phases: (1) feature extraction based on spatial feature extractor (i.e. texture feature), spectral indices (i.e. normalized burned ratio index, normalized vegetation index); (2) classification based on machine learning-based methods (support vector machine, and random forest) (Seydi et al., 2021a). These methods provided promising results but have some limitations: (1) extraction of handcrafting features and tuning them are a time-consuming process, and (2) the strength of machine learning-based methods lie in of quality and quantity of input feature dataset and sample dataset. In other words, the feature dataset (spectral and spatial features) determine the performance of machine learning methods, and (3) is more sensitive to noise condition and low generalization (Seydi et al., 2021b). In past years, deep learning-based methods have been provided promising results in many applications such as classification (Ma et al., 2021; Wu et al., 2021), change detection (Liu et al., 2021; Zhang et al., 2021d), crop mapping (Sagan et al., 2021; Xu et al., 2021a). The deep learning-based methods can extract meaningful features from the input dataset, automatically. Currently, burned area detection by deep learning-based methods have been considered and changed into hot topic research areas (Zhang et al., 2021a; Zhao et al., 2022). In this regard, many researches have been done for mapping the burned areas by remote sensing imagery.

For example, Zhang et al. (2021c) proposed a deep learning-based framework for mapping burned areas by time-series Sentinel-1 and bi-temporal Sentinel-2 images. The proposed deep learning is based on deep Siamese self-attention with share weight. They used the pre/post event Sentinel-2 images also, the temporal pre/post-fire backscatter, and coherence maps, and differencing them (differencing post-event and pre-event) as input data. Moreover, Pinto et al. (2020) proposed a deep learning-based framework for burned areas mapping using visible infrared imaging radiometer suite (VIIRS) which is called *BA-Net*. The *BA-Net* was inspired original *U-Net* with the difference that the *BA-Net* uses the Long Short-Term Memory (LSTM) and 3D kernel convolution. They used the result of burned areas with MODIS MCD64A1 product and FireCCI51 burned area product that *BA-Net* has high-efficiency compression with mentioned products. Knopp et al. (2020) designed an automatic chain processing based on a deep learning-based manner for mapping the burned areas by mono-temporal Sentinel-2 imagery. The deep learning framework is based on *U-Net* architecture and used binary cross-entropy loss function for estimation of network error in the training phase. Furthermore, they used the tapered cosine window function for overlapping prediction tiles. They reported the OA and KC were more than 98% and 0.94 in the mapping of burned areas, respectively. Hu et al. (2021) compared the efficiency of deep learning methods, machine learning classifiers, and unsupervised thresholding method on normalized burnt ratio (NBR) index using Sentinel-2 and Landsat-8 images. In this regard, they investigated four state-of-the-art deep learning methods that are included *DeepLabv3+*, *U-Net*, *FastSCNN*, and *HR-Net*. In addition, three advanced machine learning

methods Light-GBM, random forest (RF), and k-nearest neighbors (KNN) were investigated. The NBR index with Otsu thresholding and expectation maximization (EM) algorithm were implemented. The results of burned area mapping illustrate the *U-Net* method were provided the best performance by mean intersection over union (mIoU), and KC indices. Pinto et al. (2021) designed a framework for burned area mapping by the *BA-Net* and bi-temporal Sentinel-2 imagery. This framework is applied in four main phases: (1) generating burned area map by *BA-Net* and VIIRS dataset that used training deep learning model in the last phase, (2) splitting the result of burned areas into individual events, (3) preparing pre/post-event Sentinel-2 images, (4) model training based on deep learning model and resampled sample data. Farasin et al. (2020) proposed a double step *U-Net* for estimating wildfire damage severity using Sentinel-2 imagery. The mentioned proposed method uses two *U-Net* models which the first model generates the binary severity damage amp while the second *U-Net* applies for regression to estimate severity damage level. They claimed the proposed method to be robust for estimating the severity of damage in similar geological aspects. Zhang et al. (2021b) designed the near real-time wildfire progression mapping framework based on the *U-Net* model by fusion of optical and Synthetic Aperture Radar (SAR) time-series images. The time-series Sentinel-2 based burned areas before each SAR acquisition were accumulated into SAR-based pseudo progression masks to learn the *U-Net* model. Brand and Manandhar (2021) designed burned area mapping framework based on deep learning and mono-temporal Sentinel-2 imagery. The *U-Net*-based deep learning model was used for mapping the burned areas. They evaluated the potential of *U-Net* in two main scenarios: local (the model trained for each study area separately and evaluated by test areas in the same area) and global (the model trained with whole samples and evaluated on whole test areas). They reported the global scenario has high potential in the generalization model for burned area mapping in comparison with the local model. Maskouni and Seydi (2021) proposed a deep learning framework based on a convolutional neural network (CNN) and bi-temporal Sentinel-2 imagery. This framework extracts the deep features by multi-scale convolution layers then, the high-level feature explorer by single kernel convolution. They evaluated the proposed framework by stacking pre/post-event red, green, and blue bands. They reported the proposed CNN framework has high efficiency in the detection of small fire areas on a local scale. Ban et al. (2020) developed a near real-time wildfire progression monitoring framework by a CNN model using time series Sentinel-1 datasets. The generated the pseudo sample data by change detection by log-ratio and master and slave datasets. Next, the stacked pre/post-fire datasets and digital elevation (DEM) products are fed to the CNN model for monitoring of the wildfire progression. Seydi et al. (2021b) proposed a deep learning-based framework for burned area mapping by heterogeneous remote sensing datasets. They used the pre-fire Sentinel-2 imagery and post-fire hyperspectral *PRecursore IperSpettrale della Missione Applicativa* (PRISMA) imagery for mapping burned areas. This proposed deep learning framework is CNN architecture and inspired by a deep Siamese network.

The result of burned area mapping by the abovementioned deep learning-based methods is illustrated and these methods have high potential in mapping the burned areas. Furthermore, these frameworks provided promising results compared with other state-of-the-art machine learning-based methods. Howbeit, some limitations remain that motivate presenting a new framework for burned area mapping. We refer to some limitations of the abovementioned burned area mapping studies:

- (1) The most method focused on burned area mapping by change detection using bi-temporal datasets or time-series datasets. However, these methods provided promising results but extraction of burnt area information from temporal datasets is big challenging and time-consuming. Moreover, the change

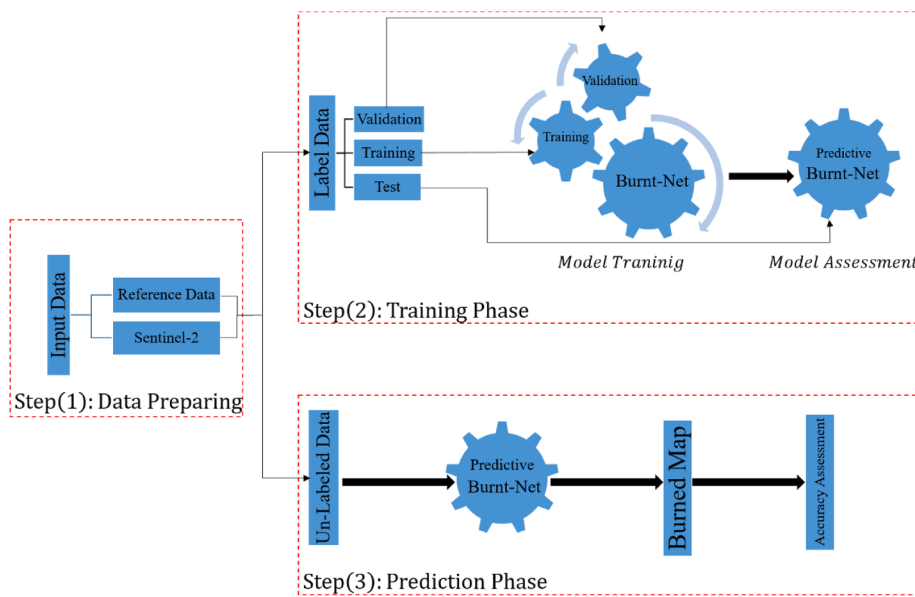


Fig. 1. Overview of the general framework for burned area mapping using the *Burnt-Net* model.

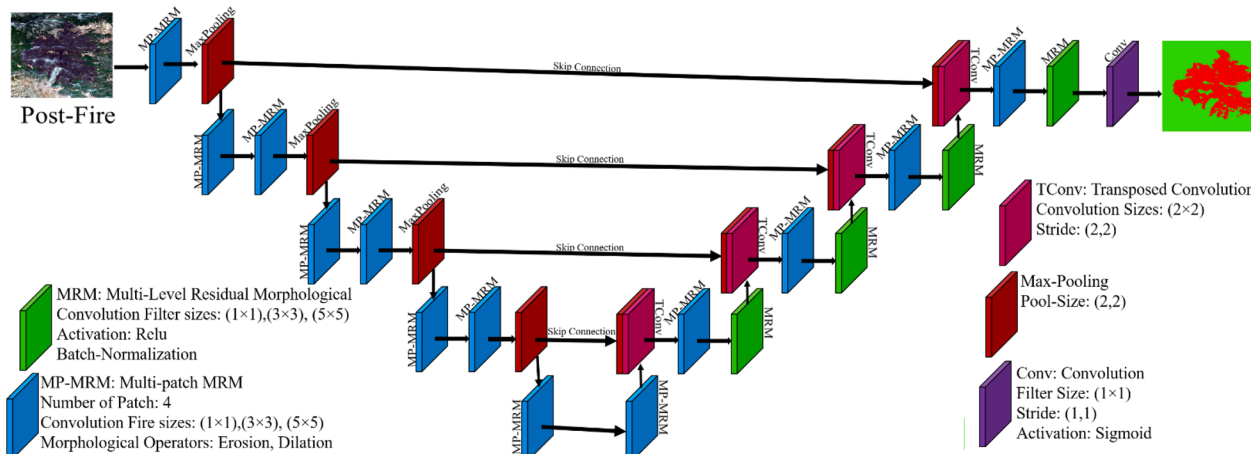


Fig. 2. Overview of the proposed *Burnt-Net* architecture for burned area mapping (BAM).

- information originated from other factors (except for the fire) that added false pixels to burned area mapping results.
- (2) The spatial resolution is the most important factor in the accurate burned area mapping that some methods focused on medium resolution datasets (more than 250 m) for burned area mapping. This theme is more evident in the accurate mapping of burned areas in small areas that are very challenging by medium-resolution datasets (i.e. MODIS, VIIRS).
 - (3) Many frameworks fused the SAR and optical datasets for burned area mapping that provided acceptable results. Although, these methods suffer high computational costs and demand for robust processing tools for extraction of burned area information. Another limitation of the fusion framework, the pre-processing (i.e. image registration) of SAR (i.e. de-speckle, multi-looking, terrain correction) and optical (atmospheric correction) datasets are very time-consuming.
 - (4) In image processing and computer vision fields, classification defines as the process of predicting a complete input based on its scores while semantic segmentation assigns labels for each input image pixel. Thus, the CNN-based classification frameworks need low sample data while requiring more time for classifying burned

areas. Furthermore, these methods suffer low generalization comparison with semantic segmentation-based methods.

- (5) Some deep learning-based frameworks used additional pre-processing (i.e. coherence map generation) or feature generation (i.e. NBR) that do not apply in an end-to-end manner and demand more time and computational costs.

In this regard, this study proposes an end-to-end deep learning-based framework for mapping burned areas to minimize the above-mentioned challenges. The proposed deep learning framework is inspired by *U-Net* architecture but has fundamental evolution in the structure of deep feature extraction. The proposed *Burnt-Net* combines the quadratic morphological learnable kernel convolution and residual blocks with standard convolution for deep feature extraction. Furthermore, the *Burnt-Net* enhances the efficiency of deep feature extraction and speed of burned area mapping by patching the input dataset. Unlike, many change detection-based burned area mapping frameworks use mon-temporal Sentinel-2 imagery for burned area mapping.

The main contribution of this research is:

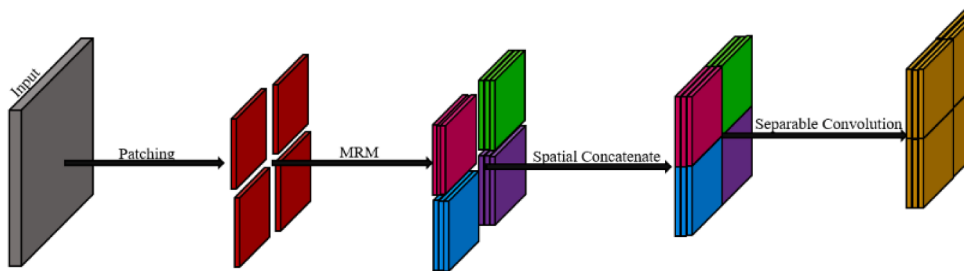


Fig. 3. The structure of the MP-MRM block.

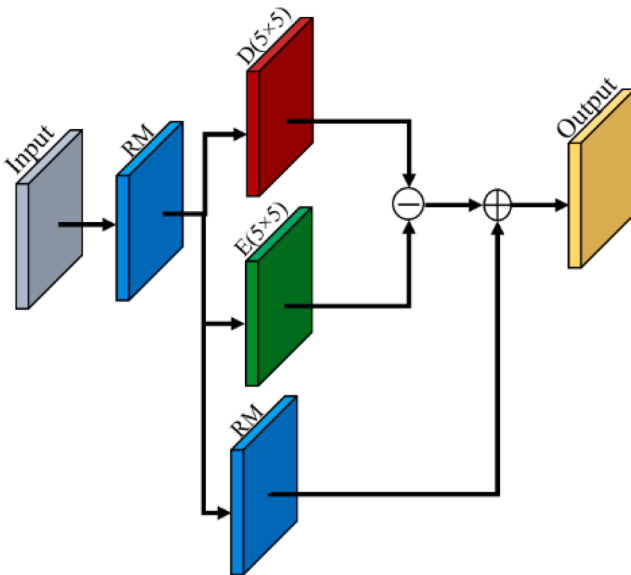


Fig. 4. The structure of MRM block.

- (1) Proposing an *End-to-End* deep learning-based framework for burned area mapping using mono-temporal high-resolution Sentinel-2 imagery (10 m).
- (2) Proposing a multi-patching scenario for enhancing processing time and deep feature extraction.
- (3) Combining the morphological learnable scale-space (i.e. quadratic dilation/erosion operators) operators and *multi-scale-residual* block the first time.
- (4) Introducing hybrid Distribution/Region-based loss functions for calculating the error of the network in the training phase.
- (5) Evaluation of the efficiency *Burnt-Net* in the mapping burned areas by different study areas also, comparison of results with state-of-the-art burnt detection deep learning-based framework.
- (6) The comparison of the coarse (MODIS MCD64A1 product) and fine (Landsat-8 burned area product) resolution burnt area products in the test areas.

The remaining part of the study is outlined as follows: **Section 2** the structure of *Burnt-Net*. **Section 3** refers to the study area and datasets. The experiments and results are provided in **Section 4**, and the discussion of the results is in **Section 5**.

2. Methodology

The proposed burned area mapping framework can be applied to the three main steps: (1) data preparing, (2) *Burnt-Net* model training, and (3) prediction based on *Burnt-Net*. The data preparation included pre-processing the Sentinel-2 dataset and patch-generation. Next, the labeled datasets are fed for the training *Burnt-Net* model. In this step, the

dataset is split into three main parts such as training, validation, and testing datasets. After tuning model parameters, the model applies for mapping burned areas and then the result of burned area mapping assesses by reference datasets. The overview of burned area mapping by the proposed method is shown in Fig. 1.

2.1. Proposed deep learning architecture

The *Burnt-Net* was inspired by *U-Net* architecture that uses the Encoder and Decoder (Fig. 2) (Ronneberger et al., 2015). The *Burnt-Net* uses the type of convolution blocks for deep feature generation. The basic operators of the proposed method are quadratic erosion, quadratic dilation, convolution, transposed convolution, separable convolution, max-pooling, batch normalization, and activation function. The encoder part builds based on multi-patch multi-level residual morphological (MP-MRM) blocks and max-pooling layers while decoder parts are built on transposed convolution, convolution layer, MP-MRM, multi-level residual morphological (MRM) blocks. More details of mentioned blocks describe in the next subsections.

The main difference between the proposed architecture with other burned mapping frameworks are:

- (1) Taking the advantage of patching help to address the problem of the processing and enhancing deep feature generation instead of using the same kernel for the whole of the scene.
- (2) Employing the trainable quadratic morphological layers can be increased the efficiency of the network in extracting nonlinear features.
- (3) Utilizing multilevel deep feature extractor and point-wise convolution in the residual block.
- (4) Using hybrid loss functions for the training of *Burnt-Net* that are based on Distribution/Region-based loss functions.

2.2. MP-MRM block

Most semantic segmentation based on methods employ a small patch size for input data (Brand and Manandhar, 2021; Chen et al., 2018; Poudel et al., 2019). However, the increase of input patch size requires a robust processor by common deep learning-based methods. This research proposed a novel framework for solving the mentioned challenges. The MP-MRM block divides the input data into some patches then, the MRM is applied to the patches (Fig. 3). Finally, the generated deep features on patches are spatially concatenated and the separable convolution layer is applied to deep features. The MP-MRM block has some advantages: (1) the feature extraction computational costs are adjusted between convolutional blocks that increase the processing time and resolve the demand for the robust processor, (2) the MP-MRM block generates the local deep feature instead of the global deep features by the same kernel for completely input patch. Fig. 3 illustrates the structure of the MP-MRM block.

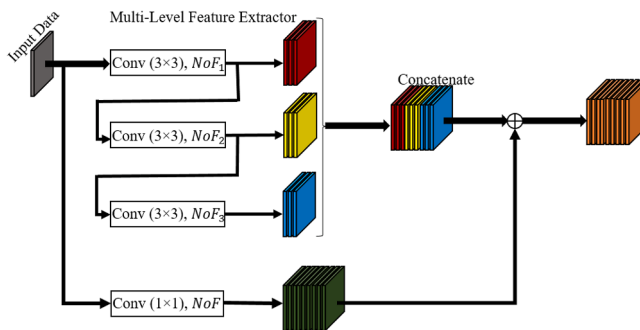


Fig. 5. Proposed residual multi-scale block.

2.3. MRM block

The MRM block is the main core of the MP-MRM block that is built on RM block and morphological operators. The MRM uses the residual morphological (RM) block, then the extracted feature is fed to the other three blocks which are the RM block, dilation, and erosion layers. The morphological operators are shape-sensitive operators and can extract non-linear deep features. The learnable erosion operator tries to focus on the background of objects while dilation concentrates on the foreground of objects. Therefore, this research combines the erosion and dilation operators for increasing the *Burnt-Net* on targets (burned areas). The output of morphological learnable operators is subtracted and added to the output of the third layer (second RM block). Fig. 4 shows the structure of the MRM block.

2.4. RM block

The RM block is almost used in *Burnt-Net* and is a basic element of the proposed architecture. Mainly, the residual block increases the efficiency of deep learning methods by providing the performance corresponding with the deeper network. Furthermore, the residual block helps to address the problem of gradient vanishing (He et al., 2016). This research proposed a multilevel residual block that is shown in Fig. 5. The RM block is formed by four convolution layers with different kernel sizes. The number of filters (NoF) in the RM block is obtained as Eq (1):

$$\begin{cases} NoF_1 = \alpha \times NoF \\ NoF_2 = \beta \times NoF \\ NoF_3 = \gamma \times NoF \\ s.t : \alpha + \beta + \gamma = 1 \end{cases} \quad (1)$$

where α, β, γ are coefficients that determine the number of filters for the first, second, and third convolution layers, respectively. These coefficients are knowledge-based and can be determined by trial and error.

2.5. Convolution layer

The convolution layers are the core building block of the deep learning methods that can learn feature representations of the input data (Goodfellow et al., 2016). A coevolution layer has built several convolution kernels to extract the type of meaningful features. This study has employed 3D/2D convolution layers for deep feature extraction (DeLancey et al., 2020; Lu et al., 2019). Mathematically, the feature value (8) in the l^{th} layer, is expressed using Eq. (2) (Seydi and Rastiveis, 2019).

$$\vartheta^l = \mathcal{F}(w^l x^{l-1}) + b^l \quad (2)$$

where x represents the input data; \mathcal{F} denotes the activation function; b represents the bias vector for the current layer, and w represents the weighted vector. The value (9) at position (x, y) on the j^{th} feature i^{th} layer for the 2D convolution layer is given by Eq. (3) (Yu et al., 2020).

$$\vartheta_{i,j}^{xy} = g \left(b_{i,j} + \sum_{\chi} \sum_{\omega=0}^{\Omega_i-1} \sum_{\varphi=0}^{\Phi_i-1} W_{i,j,\chi}^{\omega,\varphi} \vartheta_{i-1,\chi}^{(x+\omega)(y+\varphi)} \right) \quad (3)$$

where χ refers to the feature cube connected to the current feature cube in the $(i-1)^{th}$ layer, Ω , and Φ are the length, and width of the convolution kernel size, respectively.

2.6. Morphological operation layers

Morphological operators as nonlinear transformations and shape sensitive are considered an important branch of image processing (Franchi et al., 2020; Nogueira et al., 2021; Shen et al., 2019). The morphological operators are used widely in many applications such as classification (Roy et al., 2021). Recently, the learnable morphological operators have been noticed by researchers in many studies (Limonova et al., 2021; Nogueira et al., 2021).

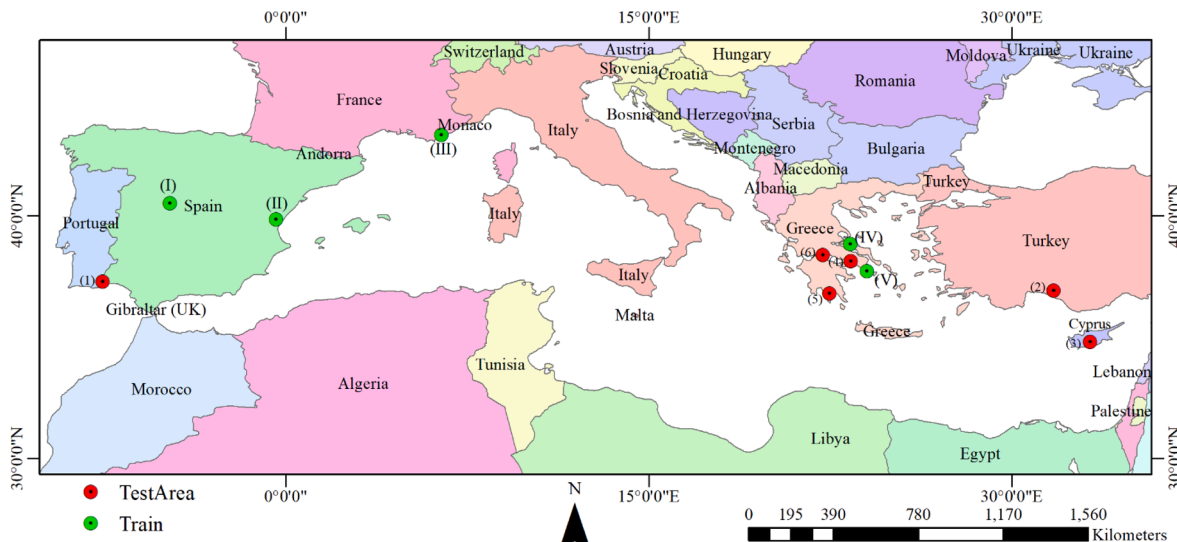


Fig. 6. The location of six study areas for burned area mapping.

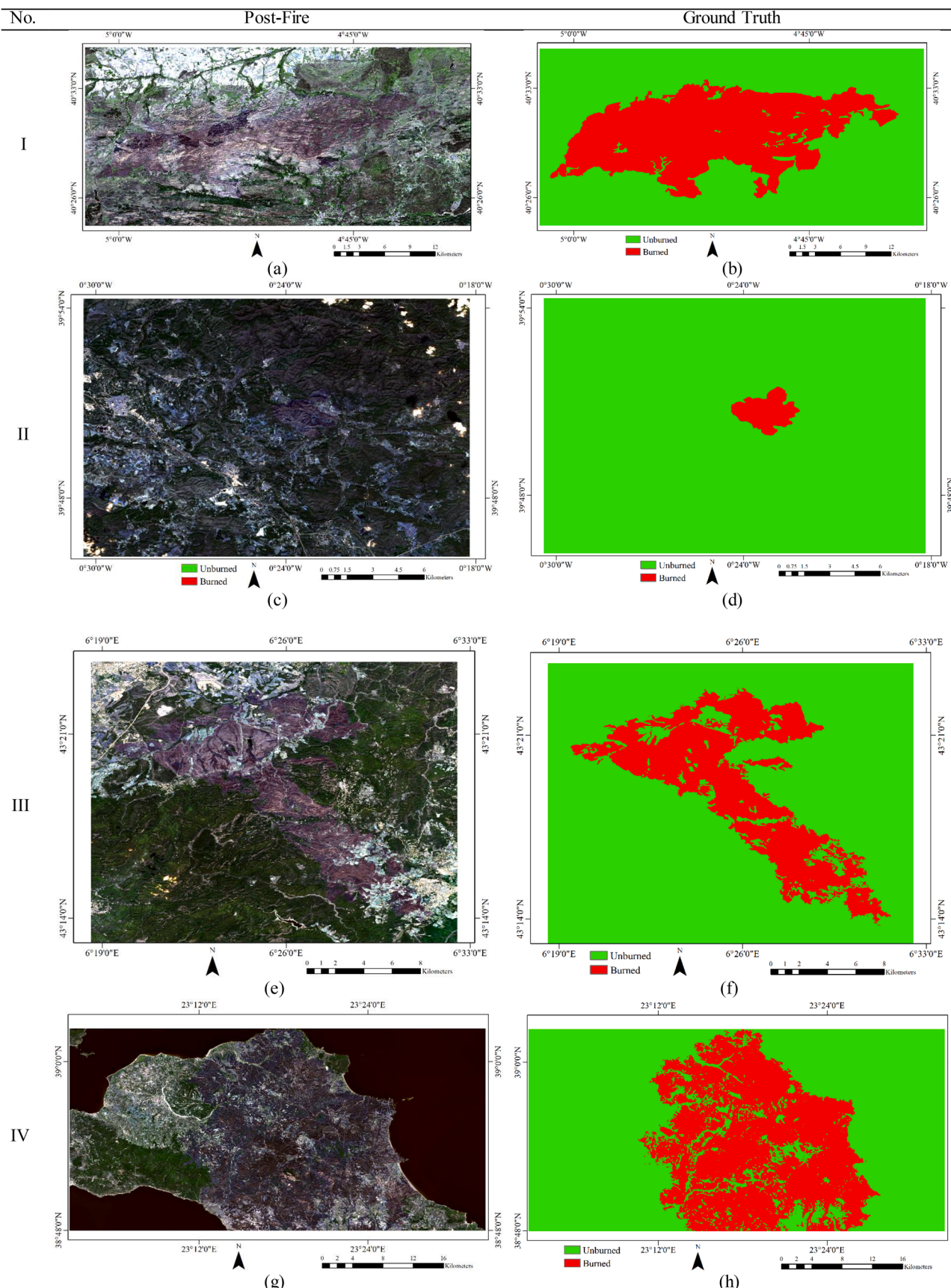


Fig. 7. The used dataset for the training model in the burned area mapping, (a) post-fire Sentinel-2, (b) ground truth for Train Area I in Fig. 6, (c) post-fire Sentinel-2, (d) ground truth for Train Area II in Fig. 6, (e) post-fire Sentinel-2, (f) ground truth for Train Area III in Fig. 6, (g) post-fire Sentinel-2, (h) ground truth for Train Area IV in Fig. 6, (i) post-fire Sentinel-2, and (j) ground truth for Train Area V in Fig. 6.

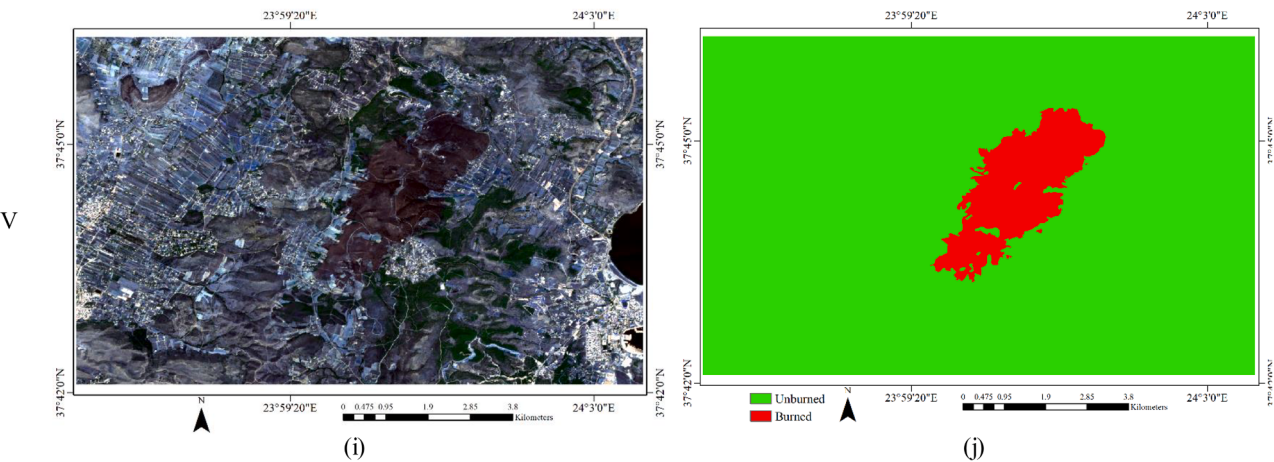


Fig. 7. (continued).

Dilation and erosion are the basic morphological operators that can extract discriminative spatial-contextual information (Islam et al., 2020; Klemen et al., 2020; Mondal, 2021). Let Ψ be image data that can be represented as a function where the intensity at position x is represented by $\Psi(x)$. Therefore, $Erosion(\epsilon_b)$ and $Dilation(\delta_b)$ by a structuring element (s) can be defined as follows (Eqs. (4), and (5)) (Franchi et al., 2020; Shen et al., 2019):

$$\epsilon_b(\Psi)(x) = \min_{i \in [-n, n]} (\Psi(x + i) - s_i) \quad (4)$$

$$\delta_b(\Psi)(x) = \min_{i \in [-n, n]} (\Psi(x - i) + s_i) \quad (5)$$

Based on the theory of morphological scale-spaces, the scalable non-flat structure functions are the most valuable function (Schmidt and Weickert, 2016). Suppose the $\tau_{n \times n}$ be a symmetric positive definite matrix thus, the quadratic structuring function associated with τ matrix is denoted as q_τ and is defined as (Eq. (6)) (Velasco-Forero et al., 2022):

$$q_\tau(\alpha) = -\frac{1}{2} \langle \alpha, \tau^{-1} \alpha \rangle \quad (6)$$

This equation for a separable and rotationally invariant structuring function can be simplified as Eq. (7) (Velasco-Forero et al., 2022):

$$q_\tau(\alpha) = -\frac{\|\alpha\|^2}{2\tau} \quad (7)$$

The erosion and dilation by a quadratic structuring function are denoted by ϵ_{q_τ} and δ_{q_τ} , respectively, which are defined Eqs. (8), (9):

$$\epsilon_{q_\tau}(\Psi)(x) = \inf_{z \in E} \left\{ \Psi(\alpha - x) + \frac{\|\alpha\|^2}{2\tau} \right\} \quad (8)$$

$$\delta_{q_\tau}(\Psi)(x) = \inf_{z \in E} \left\{ \Psi(\alpha + x) - \frac{\|\alpha\|^2}{2\tau} \right\} \quad (9)$$

The back-propagation algorithm is used to update the structural elements in the morphological layers. The propagation of gradient through the network is very similar to that of a neural network.

2.7. Training process

The error of the training model is fed to the optimizer and is updated the parameters. Due to back-propagation, the parameters are updated at each step to decrease the error of comparing the results obtained from the network with the validation dataset. This research combined the Distribution/Region-based loss functions for calculating the error of the network. To this end, a hybrid loss function has been employed that

combines the weighted cross-entropy (WCE) loss and intersection-over-union (IOU) loss (Eq. (12)).

$$Loss_{WCE}(R, P) = -\frac{1}{N} \sum_{i=1}^N \sum_{c=1}^2 w_c R_i^c \log P_i^c \quad (10)$$

$$Loss_{IOU}(R, P) = 1 - \frac{\sum_{i=1}^N \sum_{c=1}^2 R_i^c \log P_i^c}{\sum_{i=1}^N \sum_{c=1}^2 (R_i^c + P_i^c - R_i^c P_i^c)} \quad (11)$$

$$Loss(R, P) = Loss_{WCE}(R, P) + Loss_{IOU}(R, P) \quad (12)$$

where R and P are true values and predicted values, respectively. The w_c is the weight for each class, and N denotes the number of samples.

2.8. Accuracy assessment

The accuracy assessment is the most important part of burned area mapping that can be analyzed based on comparison results with a reference map. This comparison is based on interpretation by visual analysis also; the numerical measuring of the results with a reference map by standard measurement indices. In this regard, this study uses the most common measurement indices are namely overall accuracy (OA), Recall, Precision, Balance Accuracy (BC), F1-score, Jaccard index/Intersection over Union (IoU), kappa coefficient (KC), and Matthews correlation coefficient (MCC).

For comparing the performance of the proposed method, the robust deep learning-based framework has been selected for burned area mapping. This framework is based on U-Net and outperformed other state-of-the-art deep learning-based methods such as DeeplabV3+ (Chen et al., 2018), and high-resolution networks (HRNet) (Wang et al., 2020), Fast-SCNN (Poudel et al., 2019). Thus, the U-Net framework has been implemented for comparison with Burnt-Net results. More details of the U-Net model can be found in (Hu et al., 2021).

Furthermore, the Landsat burned area product (LBAP) has been selected for more evaluation of the result of Burnt-Net with other high-resolution burned area products. The Landsat-8 burnt product is generated based on the Normalized Burn Ratio Thermal (NBRT) index on each 8-day global scale. The NBRT index is defined by near-infrared, short-wave-infrared, and Thermal bands. Due to the spatial resolution of this product being 30 m, we resampled it to 15 m. In addition, assessing the result of burned area mapping by this product, the reference map was resampled to 15 m. The LBAP is based on the probability of burned areas that by thresholding convert to hard labels. The threshold value of 0.92 has been chosen for classifying and all pixels under this threshold value classify as burned pixels. It is worth noting that the optimum value of the threshold is chosen by trial error.

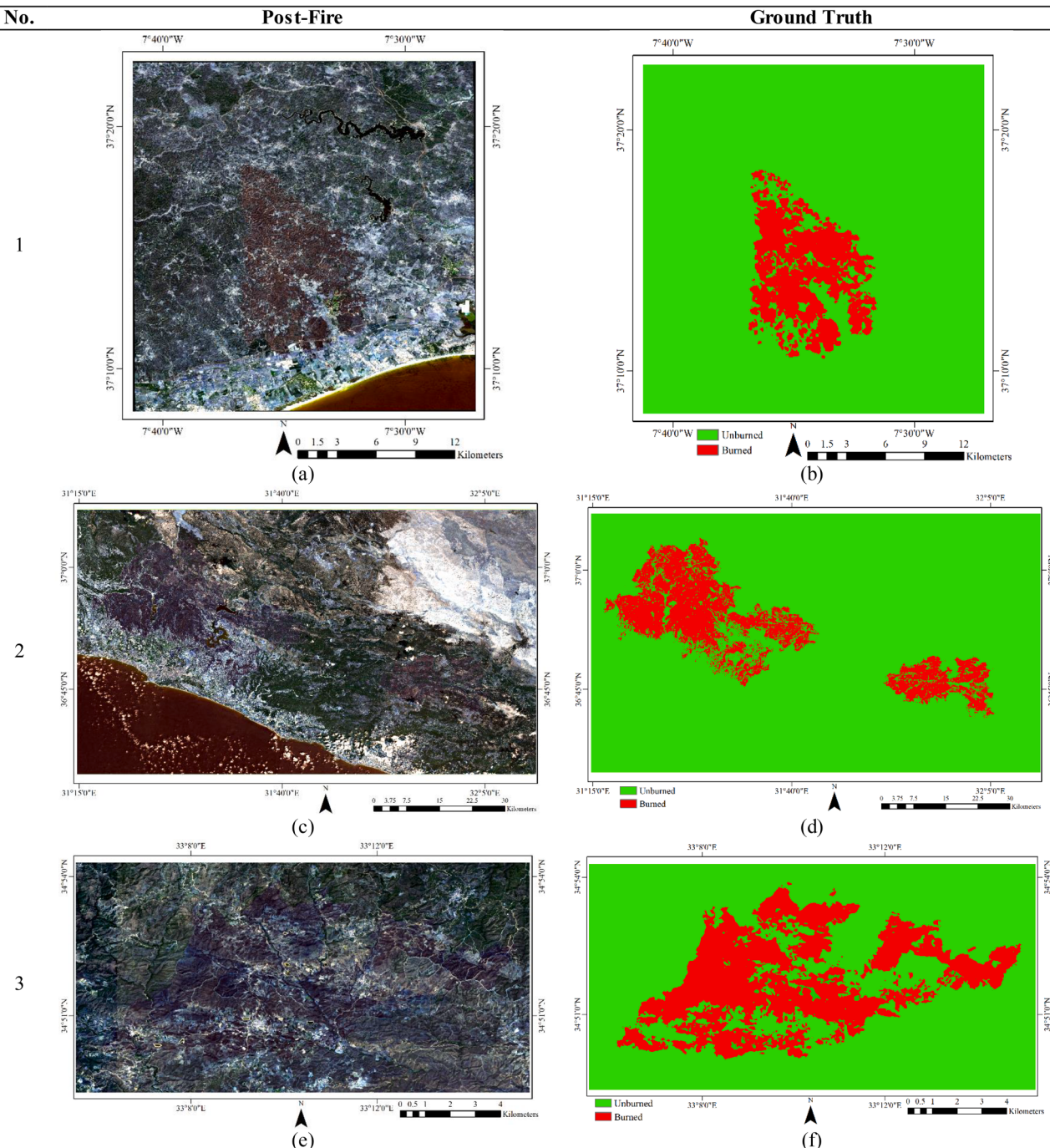


Fig. 8. The used dataset for the testing model in the burned area mapping. (a) post-fire Sentinel-2, (b) ground truth for Test Area (1 in Fig. 6.), (c) post-fire Sentinel-2, (d) ground truth for Test Area (2 in Fig. 6.), (e) post-fire Sentinel-2, (f) ground truth for Test Area (3 in Fig. 6.), (g) post-fire Sentinel-2, (h) ground truth for Test Area (4 in Fig. 6.), (i) post-fire Sentinel-2, (j) ground truth for Test Area (5 in Fig. 6.), (k) post-fire Sentinel-2, and (m) ground truth for Test Area (6 in Fig. 6.).

3. Case study and satellite images

This section investigated in more detail the case study area and satellite data.

3.1. Study area

In this study, the performance of *Burnt-Net* is evaluated using recent wildfires in some regions of the world. Furthermore, for evaluating generalization and efficiency models, we selected the different study

areas with conditions such as time of wildfires, type of land covers, and atmospheric conditions. The study areas are located in different countries, which are included: **Cyprus, Turkey, Greece, France, Portugal, and Spain**. The model was trained based on wildfires in Greece, France, and Spain while tests by located wildfires in Cyprus, Turkey, Greece, and Portugal. **Fig. 6** illustrates the location of the study areas. **The reference data is the most important factor in the evaluation of burned area mapping results**. Thus, the reference data were obtained based on visual analysis and the interpretation of the results of burned area mapping results in some papers.

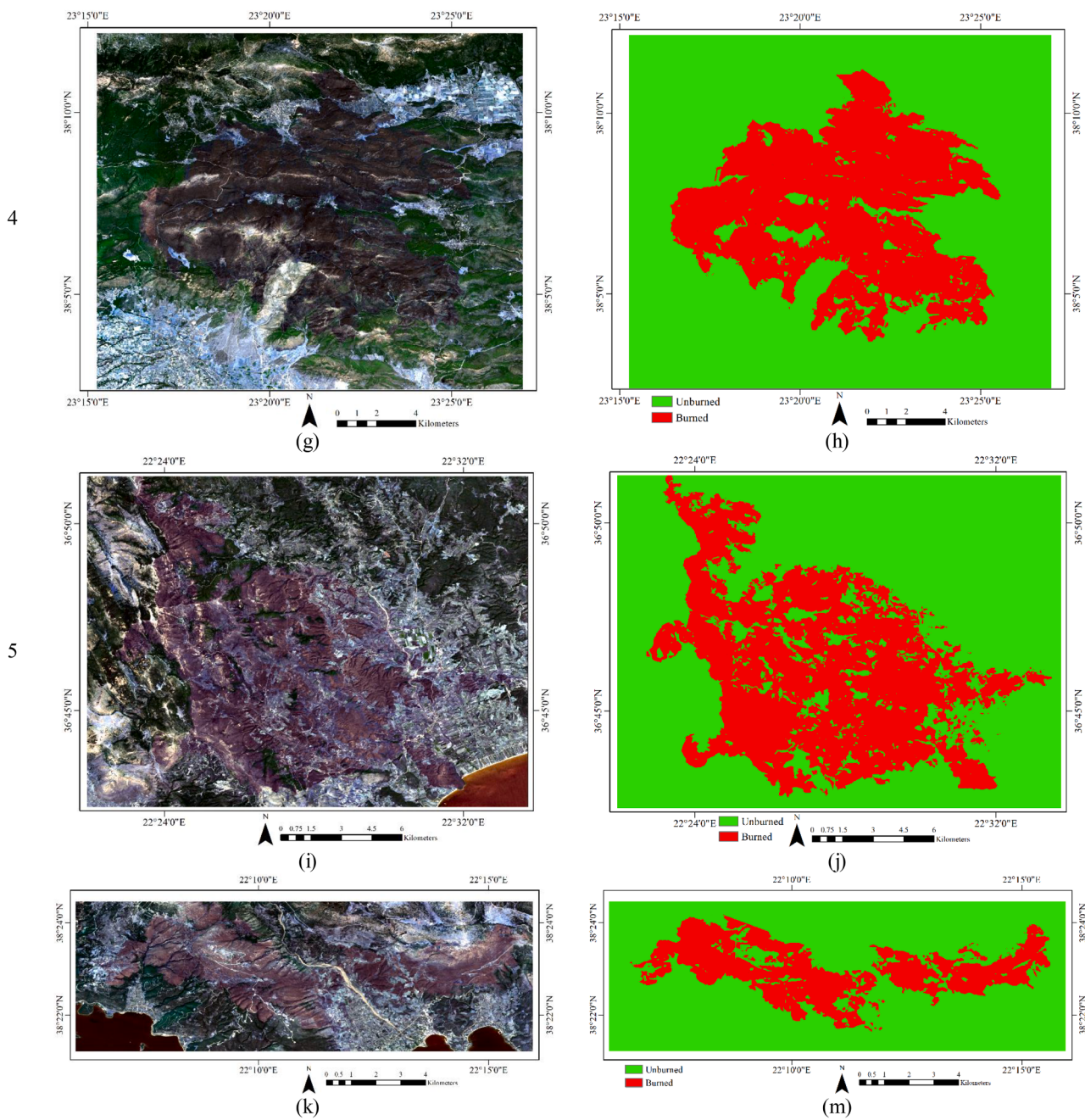


Fig. 8. (continued).

Table 1

The details of used the sample dataset for burned area mapping.

| Description | Case Study | Size Data | Unburned (pixel) | Burned (pixel) |
|-------------|------------|--------------|------------------|----------------|
| Train Area | (I) | 4547 × 2096 | 6,628,528 | 2,901,984 |
| | (II) | 2263 × 1515 | 3,364,267 | 64,178 |
| | (III) | 2585 × 1981 | 4,160,461 | 960,424 |
| | (IV) | 5489 × 2671 | 10,002,119 | 4,659,000 |
| | (V) | 1270 × 778 | 920,603 | 67,457 |
| Test Area | (I) | 2625 × 2686 | 6,301,068 | 749,682 |
| | (II) | 10488 × 6044 | 5,657,820 | 6,813,652 |
| | (III) | 1812 × 917 | 1,263,333 | 398,271 |
| | (IV) | 2172 × 1817 | 2,793,751 | 1,152,773 |
| | (V) | 2188 × 1642 | 2,437,635 | 1,155,061 |
| | (VI) | 1844 × 604 | 860,270 | 253,506 |

3.1.1. Description of Train/Validation areas

Train Area (I) Since, August 14, 2021, a large wildfire broke out near a road in Cepeda de La Mora, Spain which had taken two days. This wildfire affected the municipalities of Robledillo, Villaviciosa, Riofrío, Sotalbo and Solosancho in Castilla y León. Finally, this fire damaged the forest areas of more than 20,000 (hectares) in this area. Fig. 7-(a), (b) illustrates the color composite of the Sentinel-2 dataset.

Train Area (II) At the same time, on August 14, 2021, a forest fire began in Azuébar, located in Sierra de Espadán Natural Park, west of Spain which had taken nearly two days. Thus, this wildfire burnt more than 490 (hectares) of valuable forests in Azuébar. The color composite of the Sentinel-2 dataset is shown in Fig. 7-(c), (d).

Train Area (III) On August 16, 2021, a wildfire spread in the southern French department of VAR that has been fed by a strong mistral. This wildfire took many hours and more than 6980 (hectares) of forest and shrubland have been burned. Fig. 7-(e), (f) shows the color composite of

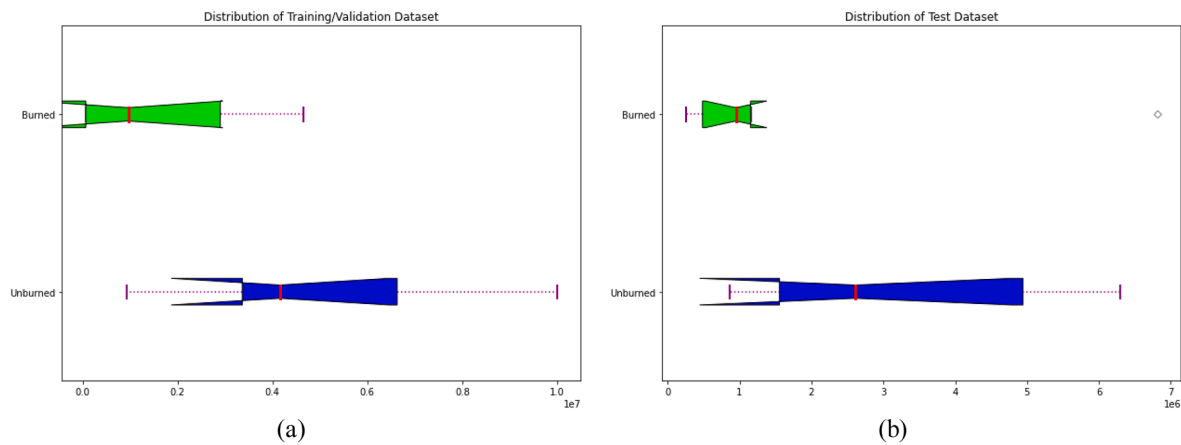


Fig. 9. Visual comparison of results of *Unburned* and *Burned* samples in Training/Validation datasets and Test dataset.

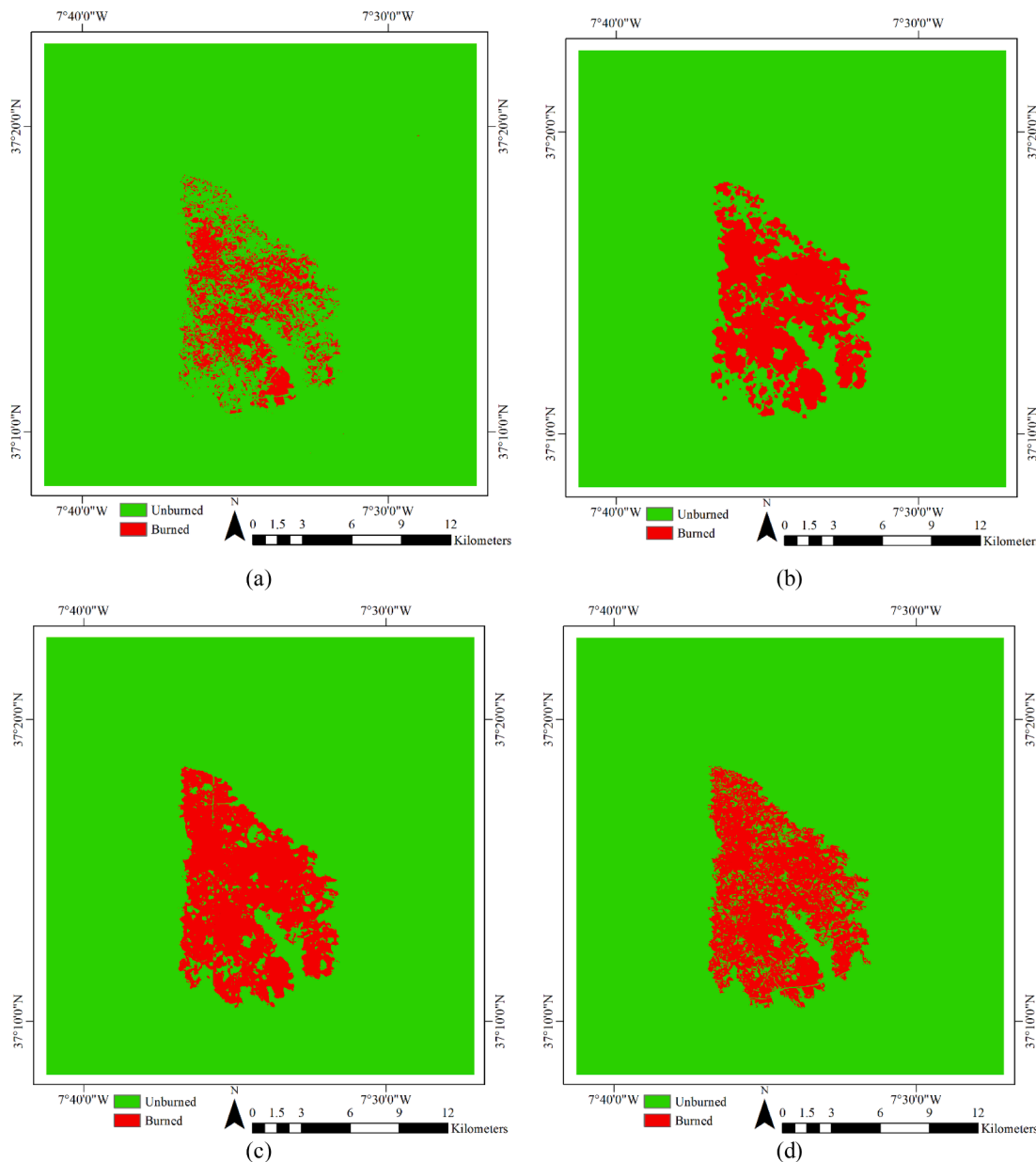


Fig. 10. Visual comparison of results of burned area mapping based on the post-event Sentinel-2 imagery and Landsat burned area product in Test Area (I): (a) LBAP, (b) U-Net, (c) Burnt-Net, and (d) ground truth map.

Table 2

Accuracy assessment of burned area mapping for Test Area (I).

| Index | LBAP | <i>U-Net</i> | Proposed-Method (<i>Burnt-Net</i>) |
|---------------|--------------|--------------|--------------------------------------|
| OA (%) | 94.66 | 96.93 | 98.08 |
| Precision (%) | 96.99 | 89.92 | 88.69 |
| Recall (%) | 0.513 | 80.16 | 93.93 |
| F1-Score (%) | 0.671 | 84.76 | 91.23 |
| BA(%) | 75.58 | 89.54 | 96.25 |
| KC | 0.645 | 0.831 | 0.902 |
| MCC | 0.684 | 0.832 | 0.902 |
| IOU | 0.505 | 0.735 | 0.839 |

the Sentinel-2 dataset and the corresponding reference map for this study area.

Train Area (IV) On August 3, 2021, a large wildfire started across Evia and the north-central region of Attica, destroying large forests in Greece. This fire continued until many hours and was intensified by strong winds that lead to the burning of more than 36,180 (hectares) of valuable forests. As seen, the color composite of the area is shown in Fig. 7-(g), (h).

Train Area (V) Since, August 17, 2021, a large wildfire began at Lavrio, in Eastern Attica, Greece. This fire continued until more than 24 h and burnt more than 530 (hectares) of the forest the color composite of this area is shown in Fig. 7-(i), (j).

3.1.2. Description of Test areas

Test Area (I) On July 15, 2021, a wildfire began spreading in the municipalities of Castro Marim and Tavira in the Faro District-Algarve, Portugal. This wildfire took more than many hours and caused the burning of about 6000 (hectares) of forest areas in this area. The color composite of the Sentinel-2 dataset for this study area is shown in Fig. 8-

(a), (b).

Test Area (II) Since, July 28, 2021, a wildfire has spread in southern Turkey, Antalya. This wildfire took some days and burnt more than 54,000 (hectares) of valuable forests in Antalya. Fig. 8-(c), (d) shows the color composite of the Sentinel-2 dataset for this study area.

Test Area (III) On July 3, 2021, a wildfire broke out in the Limassol district of Cyprus, destroying not only pine forests but also other vegetation within a few hours. This wildfire burnt more than 3200 (hectares) of forest and vegetation. Fig. 8-(e), (f) illustrates the color composite of the Sentinel-2 dataset for this study area.

Test Area (IV) On August 16, 2021, a wildfire started in the west sector of the Attica region at Pateras mountain. This fire continued for more than one day and was intensified by strong winds that lead to the burning of more than 9,000 (hectares) of the large forests. As seen, Fig. 8-(g), (h) shows the color composite of the post-fire Sentinel-2 dataset.

Test Area (V) Since, August 3, 2021, a forest fire has been raging in the municipality of East Mani in the Peloponnese region, burning down

Table 3

Accuracy assessment of burned area mapping for Test Area (II).

| Index | LBAP | <i>U-Net</i> | Proposed-Method (<i>Burnt-Net</i>) |
|---------------|--------------|--------------|--------------------------------------|
| OA (%) | 91.64 | 95.87 | 97.38 |
| Precision (%) | 99.29 | 92.43 | 96.75 |
| Recall (%) | 22.44 | 67.09 | 78.27 |
| F1-Score (%) | 36.61 | 77.75 | 86.53 |
| BA(%) | 61.21 | 83.21 | 88.97 |
| KC | 0.340 | 0.755 | 0.851 |
| MCC | 0.451 | 0.767 | 0.857 |
| IOU | 0.224 | 0.636 | 0.763 |

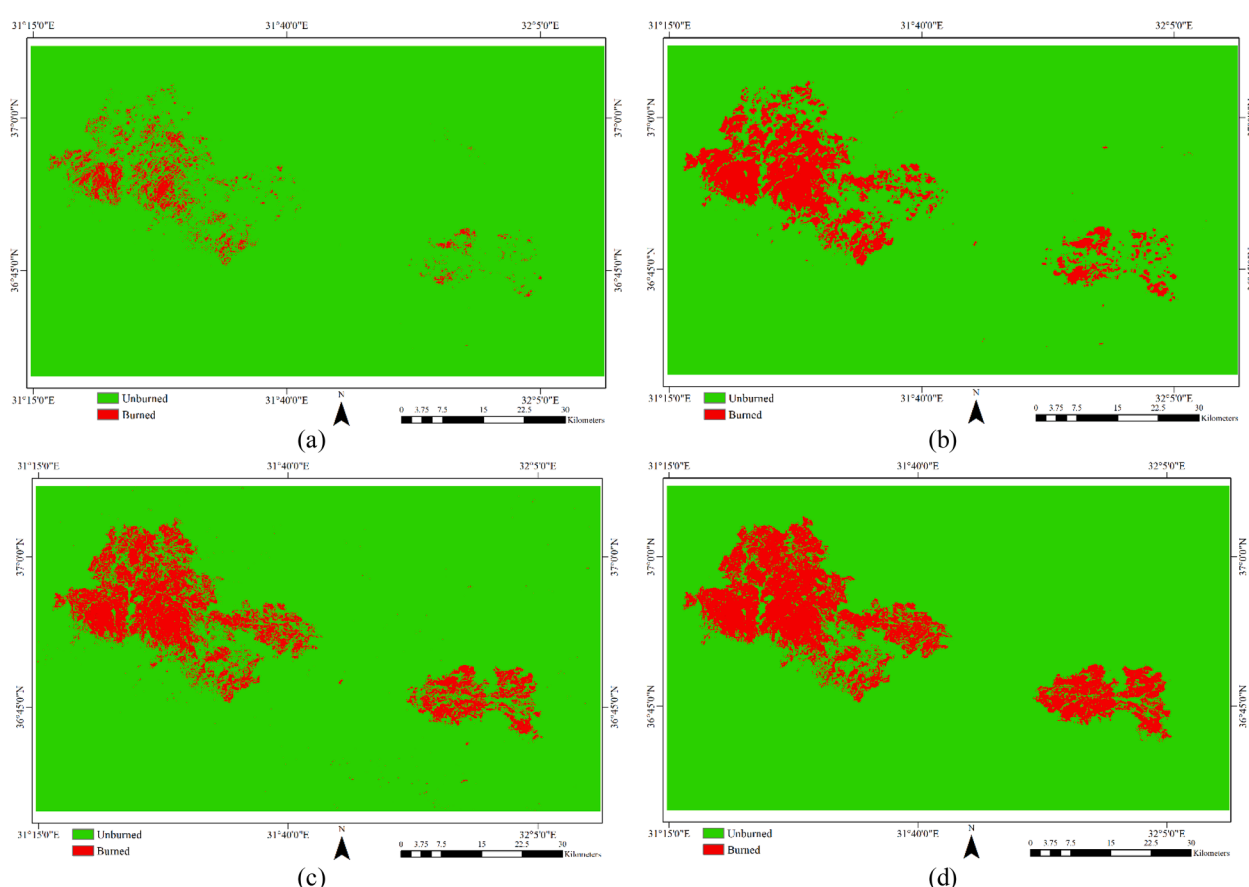


Fig. 11. Visual comparison of results of burned area mapping based on the post-event Sentinel-2 imagery and Landsat burned area product in Test Area (II): (a) LBAP, (b) *U-Net*, (c) *Burnt-Net*, and (d) ground truth map.

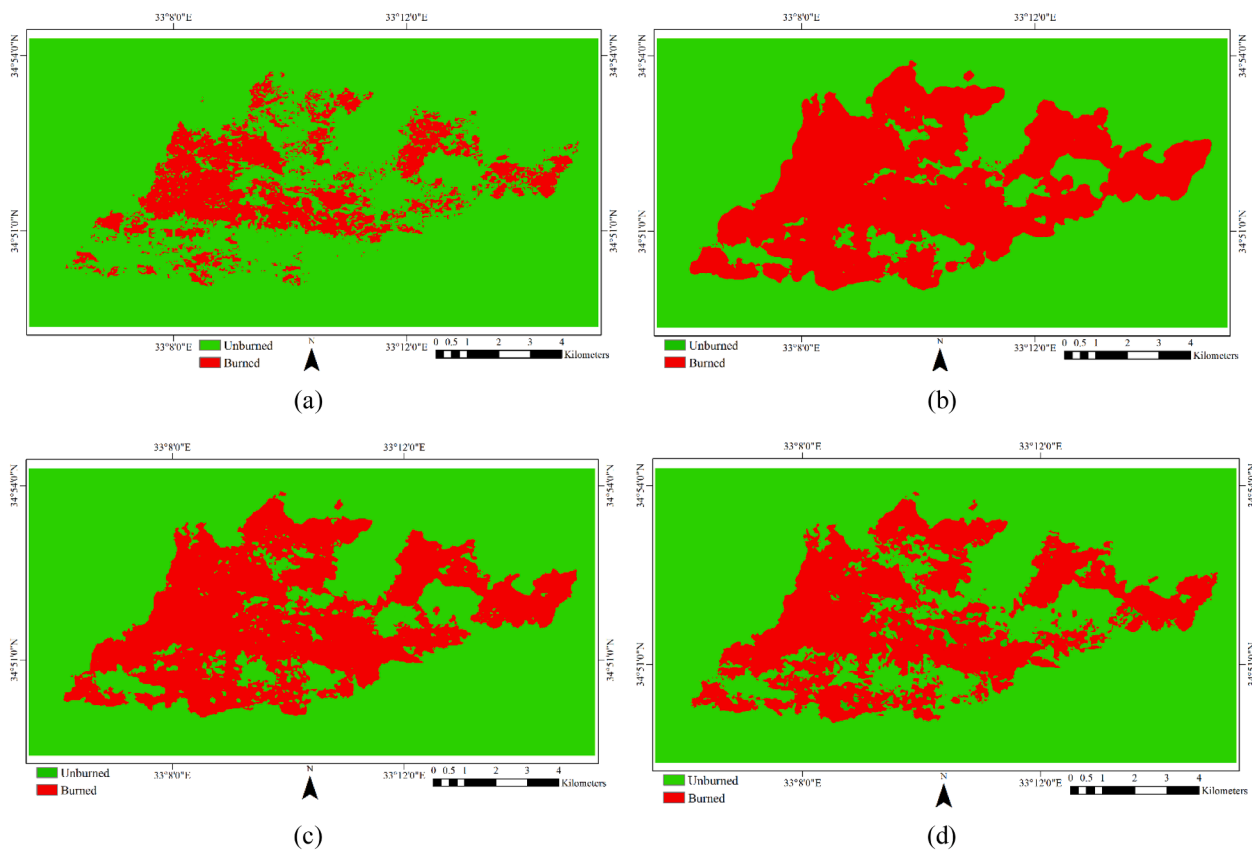


Fig. 12. Visual comparison of results of burned area mapping based on the post-event Sentinel-2 imagery and Landsat burned area product in Test Area (III): (a) LBAP, (b) U-Net, (c) Burnt-Net, and (d) ground truth map.

Table 4
Accuracy assessment of burned area mapping for Test Area (III).

| Index | LBAP | U-Net | Proposed-Method (<i>Burnt-Net</i>) |
|---------------|-------|--------------|--------------------------------------|
| OA (%) | 82.17 | 94.64 | 95.68 |
| Precision (%) | 68.34 | 87.95 | 94.32 |
| Recall (%) | 47.72 | 94.58 | 90.64 |
| F1-Score (%) | 56.02 | 91.14 | 92.44 |
| BA (%) | 70.38 | 94.62 | 94.20 |
| KC | 0.454 | 0.873 | 0.894 |
| MCC | 0.466 | 0.874 | 0.894 |
| IOU | 0.391 | 0.837 | 0.859 |

large pine forests. This fire continued until more than three days and burnt more than 9200 (hectares) of the extent forests. The color composite of the post-fire Sentinel-2 dataset is shown in Fig. 8-(i), (j).

Test Area (VI) Since, August 5, 2021, a wildfire began in Central Greece, burning down a large forest. This fire continued until about 24 h and burnt more than 1900 (hectares) of the forests. Fig. 8-(k), (m) presents the color composite of the post-fire Sentinel-2 dataset and reference map for this area.

3.2. Sentinel-2 images

Sentinel-2 is a European Space Agency (ESA) Earth observation (EO) project that performs continuous multispectral observations of the Earth's land surface at high spatial resolution. In addition to completing the Landsat and Spot missions, Sentinel-2-A and Sentinel-2-B have increased data availability for remote sensing. Each of these satellites (Sentinel-2-A and Sentinel-2-B) has a 10-day resolution, and combining them gives a 5-day resolution (Seydi et al., 2021a). The Sentinel-2 satellite acquired data at 13 spectral bands and the spatial resolution are 10

(m), 20 (m), and 60 (m) for specific spectral bands but not for all bands. In this study, the level-2A product was used as input data to map the burned areas based on surface reflectance. Table 1 shows the details of the data sets used for both study areas.

As seen, Fig. 9-(a) illustrates the distribution of sample data in the training and validation dataset. Furthermore, Fig. 9-(b) exhibits the fraction of *Unburned* and *Burned* pixels in the testing dataset. Thus, the number of *Unburned* samples is more than several *Burned* pixels that training of *Burnt-Net* applied based on imbalance dataset. To this end, this research employed a new hybrid loss function for calculating the loss value of the network.

4. Experiments and results

This section investigates the experiment and results of burned areas mapping.

4.1. Parameter setting

This study used the only spectral bands, which have 10 (m), and 20 (m) spatial resolutions for burned area mapping. The input patch size for the Sentinel-2 is $1024 \times 1024 \times 10$, the number of Epochs = 500 (epochs), weight initializer set He-normal-Initializer (He et al., 2015) for convolution layers, and also, random value for morphological layers, initial learning rate 10^{-4} , the mini-batch size is 1. The Adaptive Moment Estimation (Adam) (Kingma and Ba, 2014) optimizer is used for tuning network parameters. It is worth noticing all hyperparameters are constant during the process for the *U-Net* model. Furthermore, some Test Areas datasets have spatial dimensions lower than 1024×1024 that were filled by adding flip original dataset and after classification was changed into original size.

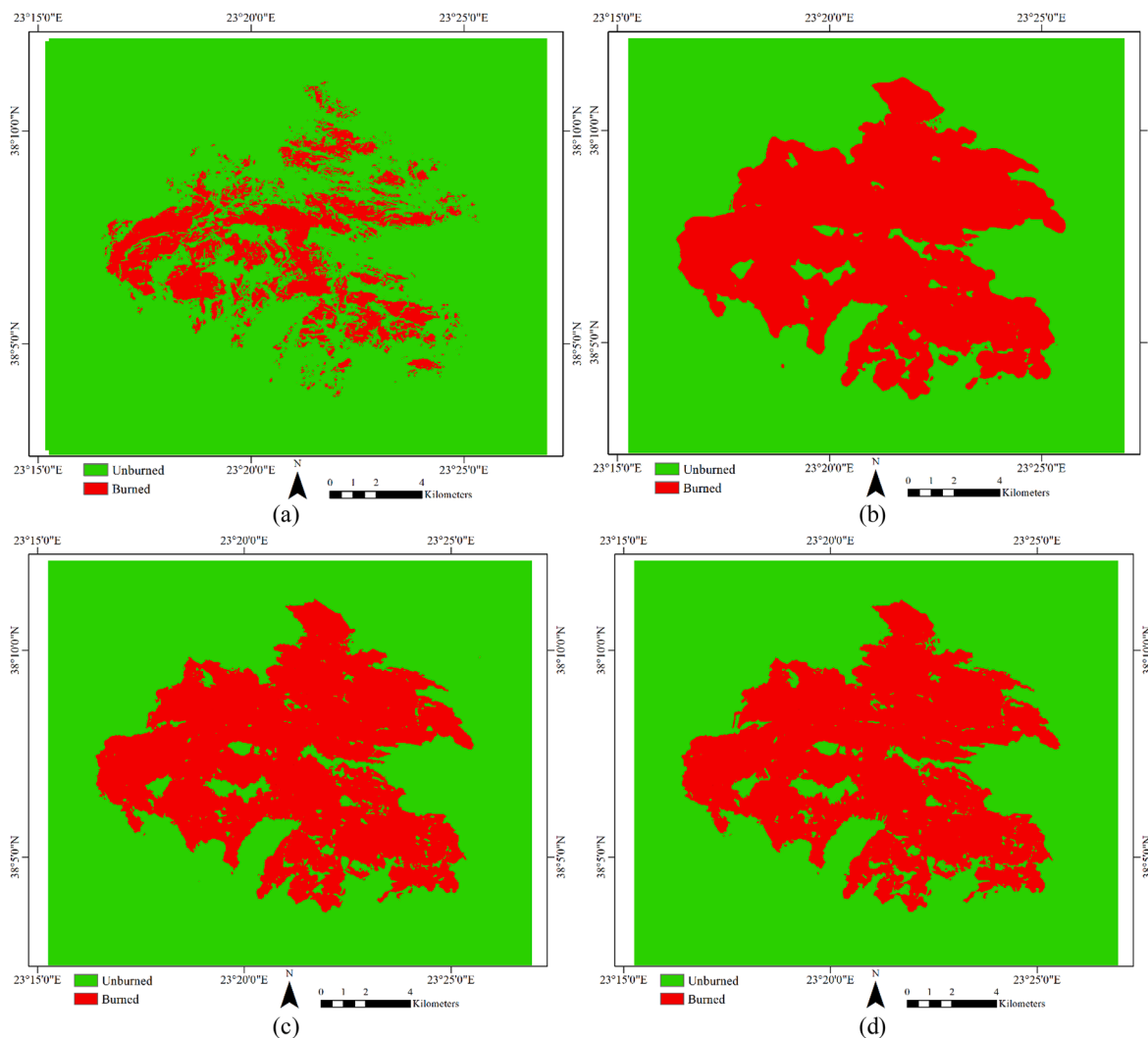


Fig. 13. Visual comparison of results of burned area mapping based on the post-event Sentinel-2 imagery and Landsat burned area product in Test Area (IV): (a) LBAP, (b) *U-Net*, (c) *Burnt-Net*, and (d) ground truth map.

Table 5
Accuracy assessment of burned area mapping for Test Area (IV).

| Index | LBAP | <i>U-Net</i> | Proposed-Method (<i>Burnt-Net</i>) |
|---------------|-------|--------------|--------------------------------------|
| OA (%) | 81.00 | 97.28 | 98.77 |
| Precision (%) | 93.19 | 92.41 | 97.36 |
| Recall (%) | 37.74 | 98.80 | 98.46 |
| F1-Score (%) | 53.73 | 95.50 | 97.91 |
| BA (%) | 68.30 | 97.72 | 98.68 |
| KC | 0.443 | 0.935 | 0.970 |
| MCC | 0.515 | 0.936 | 0.971 |
| IOU | 0.367 | 0.931 | 0.959 |

4.2. Results

4.2.1. Test area (I): Algarve, Portugal

As seen, Fig. 10 presents the result of burned area mapping based on the pre-event Sentinel-2 imagery and LBAP. The result of LBAP (Fig. 10-(a)) shows that many *burnt* pixels have been detected as *unburned* pixels. Thus, it has high miss detection pixels in comparison with deep learning-based methods while providing a low number of false pixels (Fig. 10-(a)). Based on the presented results, both methods provided promising results in the mapping of burned areas while they differ in details (Fig. 10-(b), (c)).

The numerical results of the burned area mapping for Test Area (I) are shown in Table 2. Based on numerical results, both deep learning methods had provided advanced results as; the OA is more than 96% and KC more than 0.83. The LBAP provided the high precision (96.99%) that shows high efficiency in mapping *unburned* pixels but miss its performance in mapping *burned* pixels. The *Burnt-Net* has considerably improved the results by terms Recall, KC, F1-Score, BC, MCC, and IOU. However, *Burnt-Net* provided an accuracy lower than *U-Net* by Precision index but *Burnt-Net* has significant improvement by other indices.

4.2.2. Test area (II): Antalya, Turkey

Fig. 11 illustrates the results of burned area mapping by *Burnt-Net*, *U-Net*, and LBAP for Test Area (II). The LBAP provided the low-performance result in the mapping of burnt areas because many *burnt* pixels cannot detect as well. In the visual analysis, both deep learning-based methods detected as well *unburned* areas as the results of burned areas are different. As seen, there are many miss detection pixels in the presented result by the *U-Net* model that is more evident for the second small burned area. The proposed *Burnt-Net* provided a robust result comparison with the *U-Net* model as the most *burnt* and *unburnt* pixels were detected as well.

Table 3 presents a quantitative performance comparison of the burned area detection methods for the Test Area (II). Based on this table, the LBAP detected *unburned* pixels as well (Precision 99.29%) while

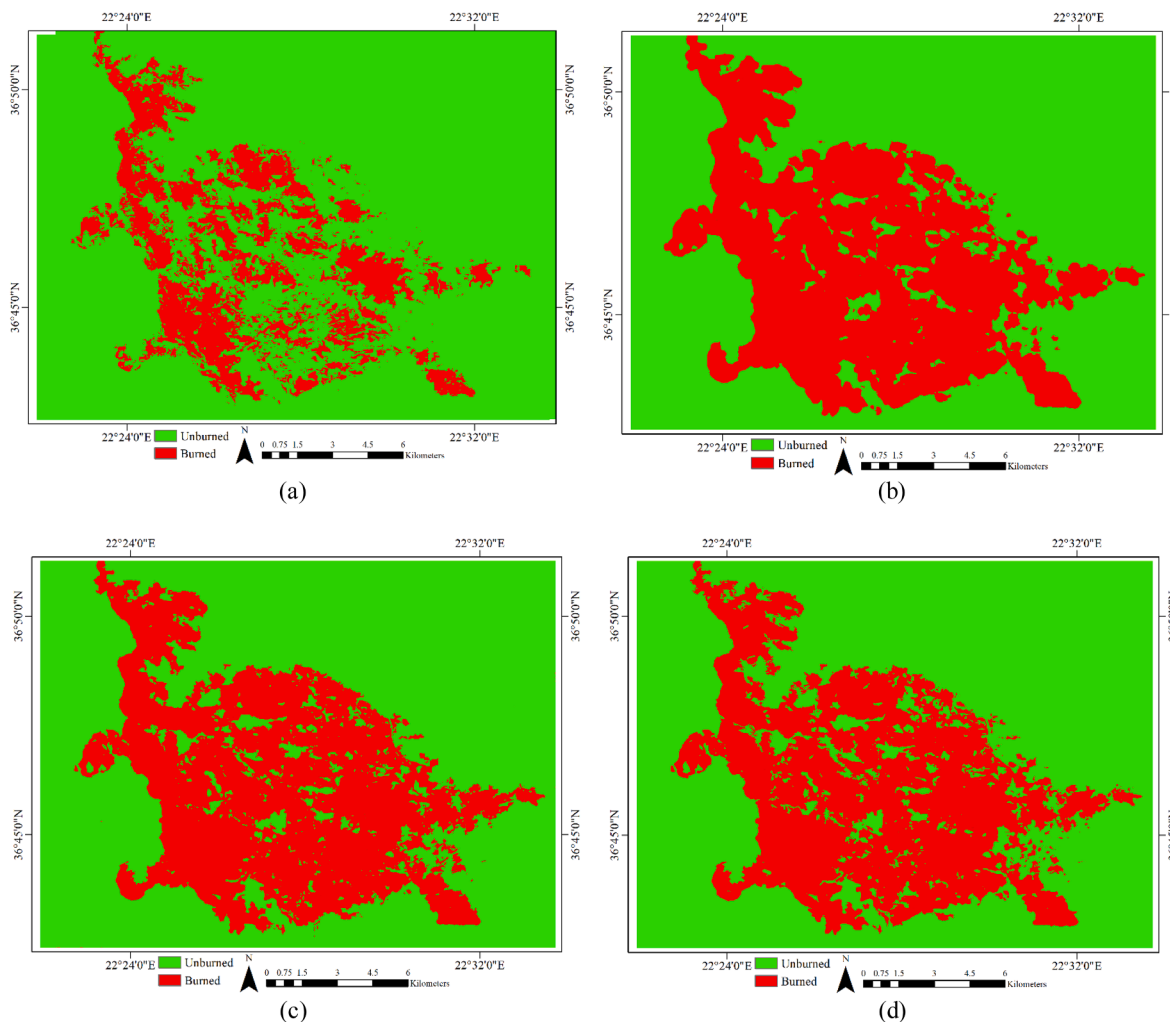


Fig. 14. Visual comparison of results of burned area mapping based on the post-event Sentinel-2 imagery and Landsat burned area product in Test Area (V): (a) LBAP, (b) U-Net, (c) Burnt-Net, and (d) ground truth map.

Table 6
Accuracy assessment of burned area mapping for Test Area (V).

| Index | LBAP | U-Net | Proposed-Method (Burnt-Net) |
|---------------|-------|-------|-----------------------------|
| OA (%) | 75.39 | 94.91 | 97.01 |
| Precision (%) | 73.81 | 88.82 | 93.29 |
| Recall (%) | 36.39 | 96.29 | 97.73 |
| F1-Score (%) | 48.75 | 92.41 | 95.46 |
| BA (%) | 65.13 | 95.27 | 97.20 |
| KC | 0.349 | 0.856 | 0.932 |
| MCC | 0.387 | 0.887 | 0.933 |
| IOU | 0.322 | 0.859 | 0.913 |

missing the performance in the detection of *burnt* pixels. It is clear; that the proposed method improved the result of burnt mapping by most indices. The efficiency of *Burnt-Net* is more evident by terms such as Recall 11%, F1-score 9%, BA 5%, KC 0.1, MCC 0.09, and IOU 0.13. Furthermore, the BC and F1-score investigate the performance of the classifier in both classes that the *Burnt-Net* outperformed considerably for both indices.

4.2.3. Test area (III): Cyprus

As seen, the result of the mapping of burned area for both deep learning models and LBAP is presented in Fig. 12 for Test Area (III). Based on the comparison of the presented results the proposed *Burnt-Net* (Fig. 12-(c)) has provided the considered results. The *U-Net* (Fig. 12-(b))

model detected some *unburned* areas as *burned* areas and this issue is more evident in the whole part of the study area. It was detected well by the LBAP (Fig. 12-(a)), but was missed by other areas. Furthermore, many small *unburned* areas have been detected by *Burnt-Net* while *U-Net* is considered as burnt areas. Thus, the proposed framework was classified in more detail while *U-Net* did focus on details.

The quantitative results of burned area mapping for Test Area (III) are shown in Table 4. As seen, the LBAP has provided a low performance compared with other deep learning-based frameworks. Based on the presented results, both deep learning-based methods have provided results considerable while the *Burnt-Net* outperformed. The *U-Net* model provided better results compared with the *Burnt-Net* model by Recall, and BA. Based on the presented results in Table 4, the *U-Net* model focused more on *burnt* pixels and this issue caused the *U-Net* model to provide a better efficiency compared with the *Burnt-Net* model. Thus, the *U-Net* has a better performance by Recall, and BA while missing its performance in the *unburned* areas.

4.2.4. Test area (IV): Western Attica, Greece

As seen, Fig. 13 illustrates the result of burned area mapping for Test Area (IV). As seen, the LBAP (Fig. 13-(a)) has provided high efficiency in the mapping of *unburned* pixels while there are many burnt pixels could not be mapped by the LBAP algorithm. Both deep learning-based methods have detected the burned and *unburned* areas as well (Fig. 13-(b), (c)). It is clear that *Burnt-Net* (Fig. 13-(c)) outperformed the

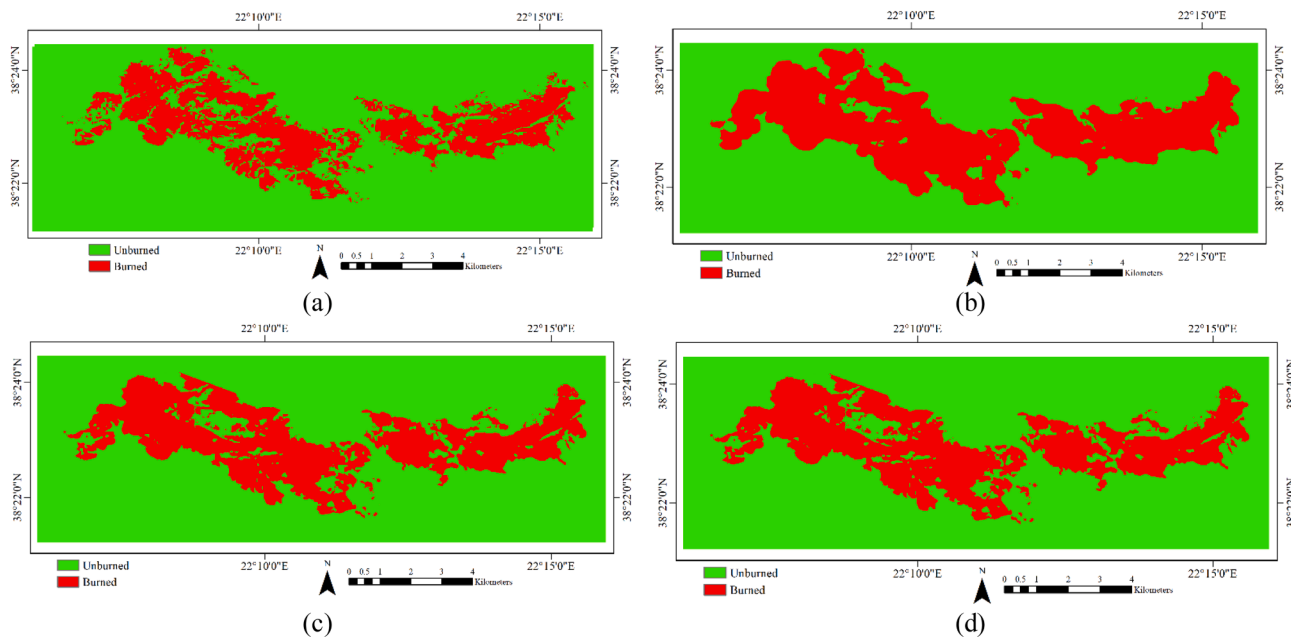


Fig. 15. Visual comparison of results of burned area mapping based on the post-event Sentinel-2 imagery and Landsat burned area product in Test Area (VI): (a) LBAP, (b) U-Net, (c) Burnt-Net, and (d) ground truth map.

Table 7
Accuracy assessment of burned area mapping for Test Area (VI).

| Index | LBAP | U-Net | Proposed-Method (Burnt-Net) |
|---------------|-------|-------|-----------------------------|
| OA (%) | 87.52 | 93.75 | 95.51 |
| Precision (%) | 76.02 | 79.14 | 84.06 |
| Recall (%) | 66.09 | 98.51 | 99.06 |
| F1-Score (%) | 70.71 | 87.77 | 90.94 |
| BA (%) | 79.97 | 95.43 | 96.76 |
| KC | 0.628 | 0.836 | 0.880 |
| MCC | 0.631 | 0.845 | 0.885 |
| IOU | 0.547 | 0.782 | 0.834 |

U-Net (Fig. 13-(b)) model by mapping in more detail. There are some *unburned* pixels as well detected by *Burnt-Net* while such areas are classified as *burnt* pixels by the *U-Net* model.

The numerical results of burned area mapping for Test Area (IV) are shown in Table 5. As seen, both methods have provided high accuracy in mapping burned areas while the *Burnt-Net* outperformed. The LBAP has provided the low performance in mapping burned areas (Recall is under 38%) while was provided the high accuracy in mapping *unburned* areas as Precision is more than 93%. The performance of the *Burnt-Net* model is more evident by more indices such as Precision 5%, F1-score 2%, KC 0.04, MCC 0.05, and IOU 0.02. However, the U-Net model had provided a bit better performance by Recall while missing its performance by other indices.

4.2.5. Test area (V): East-Mani, Greece

Fig. 14, presents the result of burned area mapping for the Test Area (V). As seen, both deep learning frameworks have provided acceptable results in the mapping of burned areas while being different in detail. Moreover, the LBAP (Fig. 14-(a)) has provided good performance in mapping burnt areas in some areas (left side of the burnt area) while other areas miss its performance (it is more evident in the center of the region of interest). Similarly, the U-Net (Fig. 14-(b)) model and *Burnt-Net* (Fig. 14-(c)) have detected more *burnt* pixels while some *unburnt* pixels have been detected as *burnt* pixels by the U-Net model. Furthermore, the *Burnt-Net* model keeps the edge of burnt areas and is more fit with ground truth.

Table 6 presents a quantitative performance comparison of the type

of methods for the Test Area (V) in the mapping burned area. Based on this table, LBAP was provided an accuracy of 75% by the OA index while other methods were provided with an accuracy of more than 94%. Moreover, there are some considerable enhancements in the results of burned area mapping in all terms in this case study area. For example, the *Burnt-Net* improved the 3% OA, 5% Precision, 0.08 KC, IOU 0.06 in burned area mapping.

4.2.6. Test area (VI): Fokida, Greece

The result of burned area mapping by *U-Net*, *Burnt-Net* models, and LBAP is shown in Fig. 15. Similarly, both methods have provided promising results in the burned area classification. Fig. 15-(a) illustrates the result of the *U-Net* model for the burned area that there are many false alarms in this result while the result of *Burnt-Net* (Fig. 15-(b)) is more fit with ground truth (Fig. 15-(c)). Furthermore, the proposed method preserves the edge of the burned areas. As seen, the LBAP has provided the more accurate result among six test areas (Fig. 14-(a)) but it has some miss detection pixels.

Table 7 presents a quantitative performance comparison of the burned area mapping for the Test Area (VI). Based on this table, the *Burnt-Net* outperformed the *U-Net* model and LBAP in all terms. The LBAP has provided an acceptable result comparison with other Test areas, as the OA is more than 87%. The improvement of *Burnt-Net* is more evident by Precision 5% and IOU 0.05, KC 0.05. Furthermore, the BC and F1-score investigated the performance of models in mapping both *burnt* and *unburnt* pixels which the *Burnt-Net* has enhanced comparison with the *U-Net* model.

4.3. Comparison with MODIS MCD64A1 product

The MCD64A1 product is burned area data that is generated based on MODIS images on a global scale. This product has a monthly temporal resolution and a spatial resolution of 500 m. The burned area mapping approach for MCD64A1 uses the active fire dataset and surface reflectance imagery. Thus, this algorithm utilizes the vegetation index and dynamic thresholding for generating the MCD64A1 burned area product. As seen, Fig. 16 presents the MCD64A1 burned area product for six test areas. Based on this, the results of the burned area by MCD64A1 product show the general structure of the burned area while missing

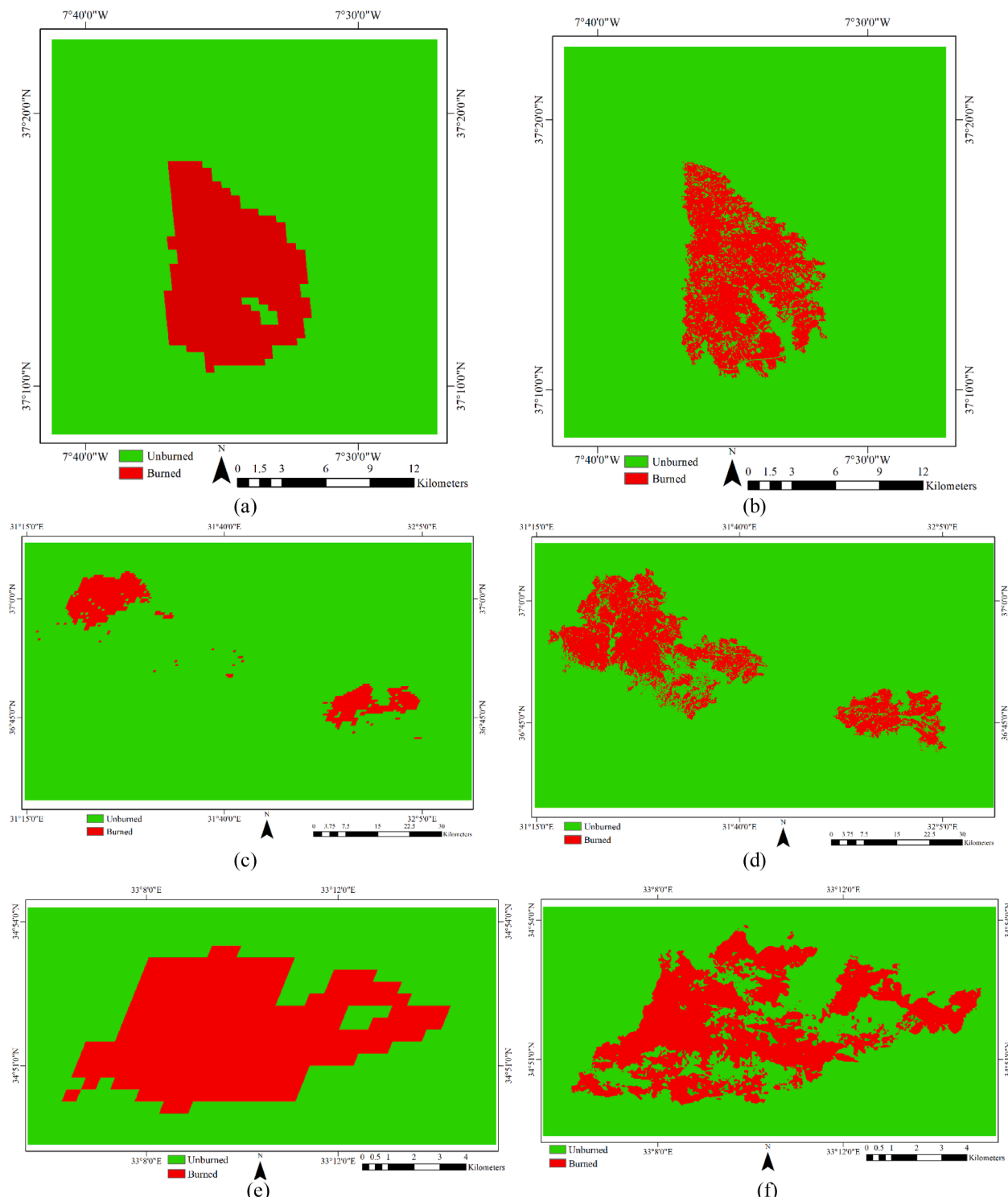


Fig. 16. Visual comparison of results of burned area mapping based on MODIS MCD64A1 Product: (a) MODIS burned area product, (b) ground truth map; for Test Area (I), (c) MODIS burned area product, (d) ground truth map; for Test Area (II), (e) MODIS burned area product, (f) ground truth map; for Test Area (III), (g) MODIS burned area product, (h) ground truth map, for Test Area (IV), (i) MODIS burned area product; (j) ground truth map, for Test Area (V), (k) MODIS burned area product, and (m) ground truth map, for Test Area (VI).

information in the details. Fig. 16 (a), (e), (g), (i), and (k) are the result of burned areas for Test areas I, II, III, IV, V, and VI, respectively which are a high number of false pixels. Furthermore, Fig. 16-(c) illustrates the result of burned area for Test Area (II) that has high miss detection pixels.

5. Discussion

This research investigated an End-to-End automatic framework for mapping burned areas based on post-fire Sentinel-2 imagery. The result of burned area mapping was obtained in six test areas and compared with other state-of-the-art burned area mapping methods and LBAP.

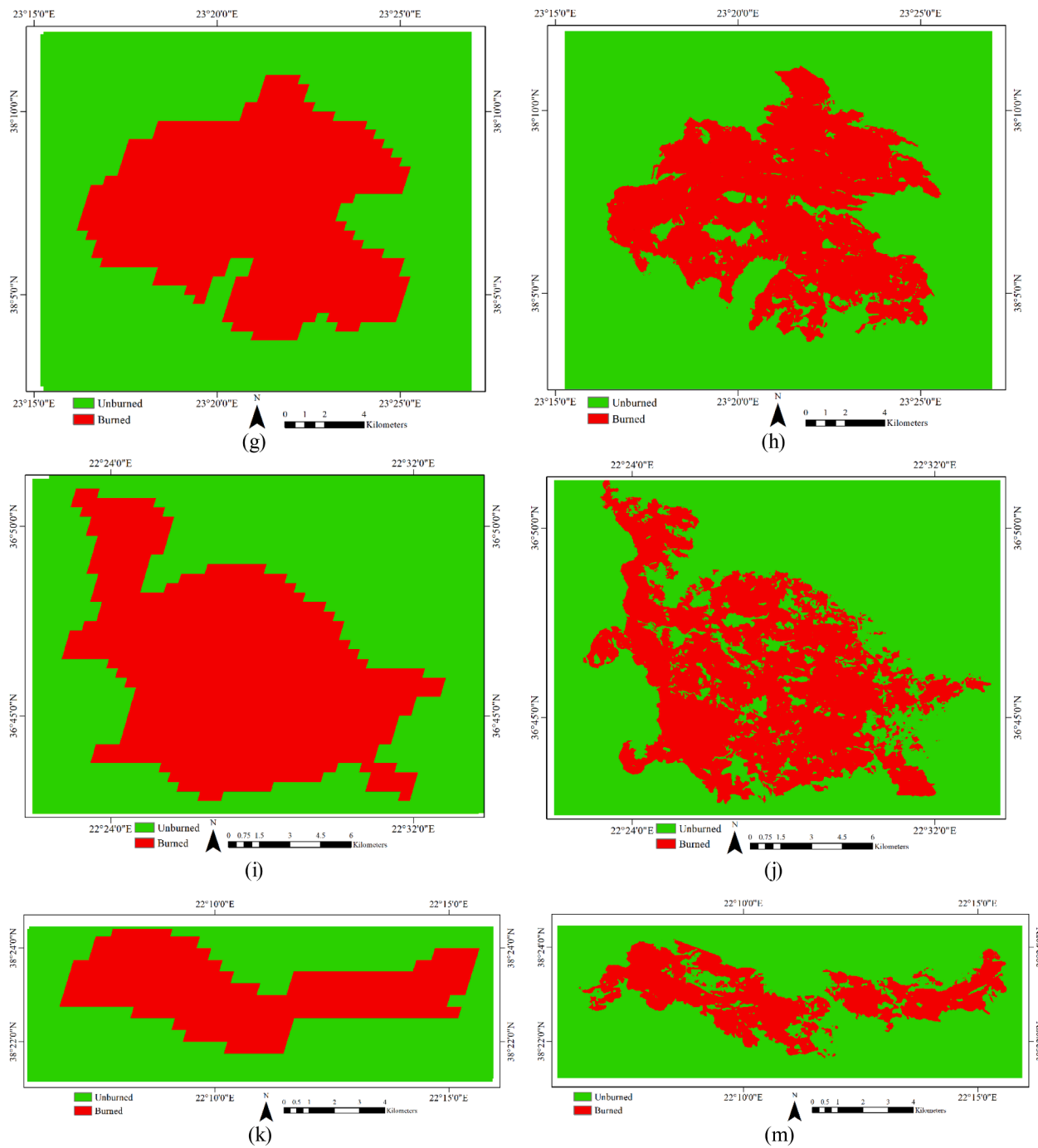


Fig. 16. (continued).

Based on visual and numerical analyses have been presented in Fig.s 10 up to 15 and Tables 2 up to 7, the deep learning-based frameworks have a high-efficiency comparison with LBAP. There are many miss detection pixels as a result of LBAP while the false pixels are very low. The Burnt-Net has provided considerable results in the detection of both *burned* and *unburned* pixels. The main difference between the Burnt-Net and U-Net models is in the detection of details that Burnt-Net can classify in more detail. As seen, Fig. 17-(a) shows the box plot of the result of burned area mapping in six test areas for LBAP, U-Net, and Burnt-Net. Based on this Fig., the LBAP has high variations in burned area mapping and the median of LBAP in the OA index is close to 85%. Due to the diversity of objects in the background, LBAP cannot detect burned areas effectively. This issue lead the LBAP to miss its performance in the mapping of

burned areas. The Burnt-Net has a compress limit box comparison with the U-Net model that shows the robustness of Burnt-Net in burned area mapping. Furthermore, the median of Burnt-Net (97.19%) is more than U-Net (95.39%) model.

Fig. 17-(b) shows the balance accuracy of the LBAP, U-Net, and Burnt-Net for test areas. Based on this Fig., the limitation of result LBAP located 62% up to 80%, and the median of LBAP is close to 85%. The LBAP shows different results in different test areas, which indicates that this product is not robust in all areas. Furthermore, the median of LBAP is close to 85%. Among deep learning-based methods, the Burnt-Net has more robustness in comparison with the U-Net model in classifying both classes. The median of the U-Net model in BA is 94.94% while Burnt-Net is 96.5%. Besides, the upper and lower limits of the boxes of Burnt-Net

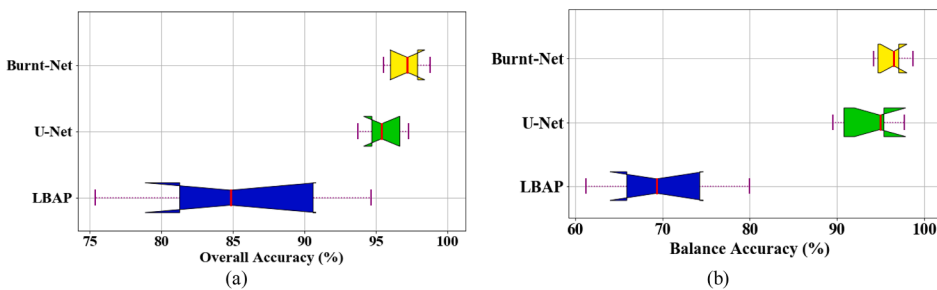


Fig. 17. Box plot showing the results of burned area mapping for LBAP, U-Net, and Burnt-Net. (a) Overall Accuracy, and (b) Balance Accuracy. The limits of the boxes indicate the lower and higher quartile. The line inside the box indicates the median. The extremities of the lines represent the minimum and maximum values obtained.

Table 8

Comparison of performance of the *Burnt-Net* with other machine learning-based frameworks.

| Reference | Index | Method | Dataset |
|--------------------------------|-----------------|---|---|
| Barboza Castillo et al. (2020) | OA: 94% | thresholding on Spectral index | Sentinel-2 |
| Syifa et al. (2020) | OA: 92% | SVM and imperialist competitive algorithm | Sentinel-2 |
| Quintano et al. (2018) | OA: 84% | Spectral index and thresholding | Combination of Landsat-8 and Sentinel-2 |
| Ngadze et al. (2020) | OA: 92% | RF | Sentinel-2 |
| Roy et al. (2019) | OA: 92% | RF change regression, and region growing manner | Combine Landsat-8 and Sentinel-2 |
| Lima et al. (2019) | OA: 96% | thresholding on Spectral index | Sentinel-2 |
| Seydi et al. (2021a) | OA: 91% | Spectral and spatial features and RF | Sentinel-2 |
| <i>Burnt-Net</i> | Mean OA: 97.07% | Deep learning-based | Sentinel-2 |

Table 9

The processing time of *Burnt-Net* in different study areas.

| Case Study | Test Area | | | | | |
|------------|-------------|--------------|------------|-------------|-------------|------------|
| | (I) | (II) | (III) | (IV) | (V) | (VI) |
| Time (S) | 5.18 | 30.23 | 2.34 | 3.50 | 3.51 | 2.27 |
| Size Data | 2625 × 2686 | 10488 × 6044 | 1812 × 917 | 2172 × 1817 | 2188 × 1642 | 1844 × 604 |

are more compact than the *U-Net* model.

Machine learning-based burned area mapping is more common in remote sensing. Recently, many frameworks have been proposed by researchers to this end. These frameworks use handcrafting features and a classifier for classification. Table 8 reports the result of burned area mapping based on advanced machine learning methods. Based on the numerical results in this table, most methods have provided an accuracy between 84% and 96% by OA index. However, the proposed method provides the mean OA of more than 97% for test areas. Thus, the *Burnt-Net* has a high-efficiency comparison with other advanced machine learning-based methods. It is worth noticing that the extraction of handcrafting features and selection of the informative feature is challenging by these methods while *Burnt-Net* extracts informative features, automatically.

The coarse resolution-based burned area products (i.e. MODIS MCD64A1) uses widely in remote sensing applications. However, these products provided a global scale and wide coverage but they suffer low spatial resolution. The detection of the small burned area by MODIS

product is very hard because the spatial resolution of these products is more than 500 m. Based on the presented results in Fig. 16, the MODIS MCD64A1 product can not detect burned areas as well while providing the general shape of burned areas. Therefore, accurate burned area mapping by such products is a big challenge. Furthermore, these products were evaluated by many researchers that provided an accuracy lower than 80% while the proposed *Burnt-Net* provides an accuracy of more than 97% by OA index. One point to be noted is that MODIS MCD64A1 products have a monthly temporal resolution while for some analysis timely burnt mapping is the most important.

The *U-Net* and *Burnt-Net* frameworks use the encoder and decoder they have provided different results. Both models trained with the same condition and sample dataset while they have provided different results in the burned area mapping. The main difference between these models is in the extraction of deep features by convolution and morphological layers. The *Burnt-Net* uses the MRM blocks that improve the efficiency of the network in the extraction of high-level deep features.

The generalization is the most important criterion in burned area mapping by remote sensing imagery. This research evaluated the performance of deep learning methods in different areas in different countries (six Test Areas). By visual and numerical analysis, the *Burnt-Net* has provided promising results for test areas. This theme shows the proposed method has high generalization in the mapping of burned areas. Table 9 provides the timely processing of the *Burnt-Net* model in six test areas. Based on this Table, the *Burnt-Net* has a high processing speed in the burned area mapping as six areas took only 47 s for mapping. This advantage of *Burnt-Net* helps to near real-time the mapping of burned areas.

6. Conclusion

The accurate and timely BAM is the most important in the mapping of the burned areas by remote sensing imagery. To this end, this study proposed a novel End-to-End automatic burned area mapping framework by post-fire Sentinel-2 imagery. The result of burned area mapping was evaluated by the latest wildfires in six different study areas in different countries. Moreover, the state-of-the-art deep learning-based method and the two most common burnt area products were considered for evaluating the performance of the proposed framework. The result of burnt area mapping shows deep learning-based models and burned area products have different performances in burned area detection. The performance of burned areas depends on the complexity of the regions of interest and objects. The result of burnt area mapping shows that *Burnt-Net* has high efficiency in the accurate and timely mapping of burned areas. The proposed method provides an accuracy of more than 97% for test areas while other methods provided an accuracy lower than 95%. Besides, the LBAP has high miss detection and false pixels in the different areas. The MODIS MCD64A1 product provides the main shape of burned areas while not being able to detect burned areas in more detail. Based on numerical and visual analysis, the *Burnt-Net* has some advantages in comparison with other state-of-the-art methods: (1)

it provides the burned area map more accurate than other products and methods, (2) it provides robust results compared with a *U-Net* model, (3) utilizes only post-fire dataset, (4) can be applied in the End-to-End framework requires no pre-processing, and (5) the *Burnt-Net* is fast and can generate the burned area in the near real-time.

CRediT authorship contribution statement

Seyd Teymoor Seydi: Conceptualization, Methodology, Writing – original draft. **Mahdi Hasanlou:** Supervision, Writing – original draft, Methodology. **Jocelyn Chanussot:** Supervision, Writing – original draft.

Declaration of Competing Interest

The authors declare that they have no known competing financial interests or personal relationships that could have appeared to influence the work reported in this paper.

References

- Ahmad, M., Shabbir, S., Roy, S.K., Hong, D., Wu, X., Yao, J., Khan, A.M., Mazzara, M., Distefano, S., Chanussot, J., 2021. Hyperspectral Image Classification—Traditional to Deep Models: A Survey for Future Prospects. *IEEE J. Sel. Top. Appl. Earth Observ. Remote Sensing* 15, 968–999.
- Ban, Y., Zhang, P., Nascetti, A., Bevington, A.R., Wulder, M.A., 2020. Near real-time wildfire progression monitoring with Sentinel-1 SAR time series and deep learning. *Sci. Rep.* 10, 1–15.
- Barboza Castillo, E., Turpo Cayo, E., de Almeida, C., Salas López, R., Rojas Briceño, N., Silva López, J., Barrena Gurbillón, M., Oliva, M., Espinoza-Villar, R., 2020. Monitoring wildfires in the northeastern peruvian amazon using landsat-8 and sentinel-2 imagery in the GEE platform. *ISPRS Int. J. Geo-Inf.* 9 (10), 564.
- Boschetti, L., Roy, D.P., Giglio, L., Huang, H., Zubkova, M., Humber, M.L., 2019. Global validation of the collection 6 MODIS burned area product. *Remote sensing of environment* 235: 111490.
- Boschetti, L., Stehman, S.V., Roy, D.P., 2016. A stratified random sampling design in space and time for regional to global scale burned area product validation. *Remote Sens. Environ.* 186, 465–478.
- Brand, A., Manandhar, A., 2021. Semantic segmentation of burned areas in satellite images using a U-net-based convolutional neural network. *Int. Arch. Photogrammetry, Remote Sens. Spatial Inf. Sci.* 43, 47–53.
- Campagnolo, M., Libonati, R., Rodrigues, J., Pereira, J., 2021. A comprehensive characterization of MODIS daily burned area mapping accuracy across fire sizes in tropical savannas. *Remote Sens. Environ.* 252, 112115.
- Cardil, A., Rodrigues, M., Ramirez, J., de-Miguel, S., Silva, C.A., Mariani, M., et al., 2021. Coupled effects of climate teleconnections on drought, Santa Ana winds and wildfires in southern California. *Sci. Total Environ.* 765, 142788.
- Chen, L.-C., Zhu, Y., Papandreou, G., Schroff, F., Adam, H., 2018. Encoder-decoder with atrous separable convolution for semantic image segmentation. In: Proceedings of the European conference on computer vision (ECCV), pp. 801–818.
- Chuvieco, E., Yue, C., Heil, A., Moullot, F., Alonso-Canas, I., Padilla, M., Pereira, J.M., Oom, D., Tansey, K., 2016. A new global burned area product for climate assessment of fire impacts. *Global Ecol. Biogeogr.* 25 (5), 619–629.
- DeLancey, E.R., Simms, J.F., Mahdianpari, M., Brisco, B., Mahoney, C., Kariyeva, J., 2020. Comparing deep learning and shallow learning for large-scale wetland classification in Alberta, Canada. *Remote Sens.* 12, 2.
- ElGharbawi, T., Zarzoura, F., 2021. Damage detection using SAR coherence statistical analysis, application to Beirut, Lebanon. *ISPRS J. Photogrammetry Remote Sensing* 173, 1–9.
- Farasin, A., Colombo, L., Garza, P., 2020. Double-step u-net: A deep learning-based approach for the estimation of wildfire damage severity through sentinel-2 satellite data. *Appl. Sci.* 10, 4332.
- Franchi, G., Fehri, A., Yao, A., 2020. Deep morphological networks. *Pattern Recognit.* 102, 107246.
- Franquesa, M., Lizundia-Loiola, J., Stehman, S.V., Chuvieco, E., 2022. Using long temporal reference units to assess the spatial accuracy of global satellite-derived burned area products. *Remote Sens. Environ.* 269, 112823.
- Gajardo, J., Mora, M., Valdés-Nicolao, G., Carrasco-Benavides, M., 2022. Burned Area Classification Based on Extreme Learning Machine and Sentinel-2 Images. *Appl. Sci.* 12, 9.
- Goodfellow, I., Bengio, Y., Courville, A., 2016. Deep learning. MIT Press.
- Hawbaker, T.J., Vanderhoof, M.K., Schmidt, G.L., Beal, Y.-J., Picotte, J.J., Takacs, J.D., et al., 2020. The Landsat Burned Area algorithm and products for the conterminous United States. *Remote Sens. Environ.* 244, 111801.
- He, K., Zhang, X., Ren, S., Sun, J., 2015. Delving deep into rectifiers: Surpassing human-level performance on imagenet classification. In: Proceedings of the IEEE international conference on computer vision, pp. 1026–1034.
- He, K., Zhang, X., Ren, S., Sun, J., 2016. Deep residual learning for image recognition. In: Proceedings of the IEEE conference on computer vision and pattern recognition, pp. 770–778.
- Hu, X., Ban, Y., Nascetti, A., 2021. Uni-temporal multispectral imagery for burned area mapping with deep learning. *Remote Sensing* 13, 1509.
- Islam, M.A., Murray, B., Buck, A., Anderson, D.T., Scott, G.J., Popescu, M., Keller, J., 2020. Extending the morphological hit-or-miss transform to deep neural networks. *IEEE Trans. Neural Networks Learning Syst.* 32 (11), 4826–4838.
- Kingma, D.P., Ba, J., 2014. Adam: A method for stochastic optimization. arXiv preprint arXiv:1412.6980 2014.
- Klemen, M., Krsnik, L., Robnik-Sikonja, M., 2020. Enhancing deep neural networks with morphological information. arXiv preprint arXiv:12432 2020.
- Knopp, L., Wieland, M., Rätsch, M., Martinis, S., 2020. A deep learning approach for burned area segmentation with Sentinel-2 data. *Remote Sens.* 12, 2422.
- Lima, T.A., Beuchle, R., Langner, A., Grecchi, R.C., Griess, V.C., Achard, F., 2019. Comparing Sentinel-2 MSI and Landsat 8 OLI imagery for monitoring selective logging in the Brazilian Amazon. *Remote Sens.* 11, 961.
- Limonova, E.E., Alfonso, D.M., Nikolaev, D.P., Arlazarov, V.V., 2021. Bipolar morphological neural networks: gate-efficient architecture for computer vision. *IEEE Access* 9, 97569–97581.
- Liu, T., Yang, L., Lunga, D., 2021. Change detection using deep learning approach with object-based image analysis. *Remote Sens. Environ.* 256, 112308.
- Lu, L., Wang, X., Carneiro, G., Yang, L., 2019. Deep learning and convolutional neural networks for medical imaging and clinical informatics. Springer.
- Luppichini, M., Barsanti, M., Giannecchini, R., Bini, M., 2022. Deep learning models to predict flood events in fast-flowing watersheds. *Sci. Total Environ.* 813, 151885.
- Ma, A., Wan, Y., Zhong, Y., Wang, J., Zhang, L., 2021. SceneNet: Remote sensing scene classification deep learning network using multi-objective neural evolution architecture search. *ISPRS J. Photogrammetry Remote Sens.* 172, 171–188.
- Maskouni, F.H., Seydi, S.T., 2021. Forest Burned Area Mapping Using Bi-Temporal Sentinel-2 Imagery Based on a Convolutional Neural Network: Case Study in Golestan Forest. *Eng. Proc.* 10, 6.
- McCorkel, J., Montanaro, M., Efremova, B., Pearlman, A., Wenny, B., Lunsford, A., et al., 2018. Landsat 9 thermal infrared sensor 2 characterization plan overview. In: IGARSS 2018–2018 IEEE International Geoscience and Remote Sensing Symposium, pp. 8845–8848.
- Michael, Y., Helman, D., Glickman, O., Gabay, D., Brenner, S., Lensky, I.M., 2021. Forecasting fire risk with machine learning and dynamic information derived from satellite vegetation index time-series. *Sci. Total Environ.* 764, 142844.
- Mondal, R., 2021. Morphological Network: Network With Morphological Neurons. Indian Statistical Institute-Kolkata.
- Moresi, D., Marzano, R., Lingua, E., Motta, R., Garbarino, M., 2022. Mapping burn severity in the western Italian Alps through phenologically coherent reflectance composites derived from Sentinel-2 imagery. *Remote Sens. Environ.* 269, 112800.
- Muñoz, D.F., Muñoz, P., Moftakhari, H., Moradkhani, H., 2021. From local to regional compound flood mapping with deep learning and data fusion techniques. *Sci. Total Environ.* 782, 146927.
- Naderpour, M., Rizeei, H.M., Ramezani, F., 2021. Forest fire risk prediction: a spatial deep neural network-based framework. *Remote Sens.* 13, 2513.
- Ngadze, F., Mpakairi, K.S., Kavhu, B., Ndaimani, H., Maremba, M.S., 2020. Exploring the utility of Sentinel-2 MSI and Landsat 8 OLI in burned area mapping for a heterogeneous savannah landscape. *PLoS one* 15, e0232962.
- Nogueira, K., Chanussot, J., Dalla Mura, M., Dos Santos, J.A., 2021. An introduction to deep morphological networks. *IEEE Access* 9, 114308–114324.
- Otón, G., Franquesa, M., Lizundia-Loiola, J., Chuvieco, E., 2021. Validation of low spatial resolution and no-dichotomy global long-term burned area product by pareto boundary. *Earth Resources and Environmental Remote Sensing/GIS Applications XII*. 11863. SPIE, pp. 293–299.
- Otón, G., Lizundia-Loiola, J., Pettinari, M.L., Chuvieco, E., 2021b. Development of a consistent global long-term burned area product (1982–2018) based on AVHRR-LTD data. *Int. J. Appl. Earth Observ. Geoinf.* 103, 102473.
- Pilger, C., Hupe, P., Gaebler, P., Kalia, A., Schneider, F., Steinberg, A., et al., 2020. Yield estimation of the 2020 Beirut explosion using open access waveform and remote sensing data. 2020.
- Pinto, M.M., Libonati, R., Trigo, R.M., Trigo, I.F., DaCamara, C.C., 2020. A deep learning approach for mapping and dating burned areas using temporal sequences of satellite images. *ISPRS J. Photogrammetry Remote Sens.* 160, 260–274.
- Pinto, L.C., Sousa, S., Valente, M., 2022. Economic valuation under different informational contexts. *Energy Policy* 161112765.
- Pinto, M.M., Trigo, R.M., Trigo, I.F., DaCamara, C.C., 2021. A Practical Method for High-Resolution Burned Area Monitoring Using Sentinel-2 and VIIRS. *Remote Sens.* 13, 1608.
- Poudel, R.P., Liwicki, S., Cipolla, R., 2019. Fast-scnn: Fast semantic segmentation network. arXiv preprint arXiv:1902.04502.
- Quintano, C., Fernández-Manso, A., Fernández-Manso, O., 2018. Combination of Landsat and Sentinel-2 MSI data for initial assessing of burn severity. *Int. J. Appl. Earth Observ. Geoinf.* 64, 221–225.
- Radočaj, D., Jurišić, M., Gašparović, M., 2022. A wildfire growth prediction and evaluation approach using Landsat and MODIS data. *J. Environ. Manage.* 304, 114351.
- Ronneberger, O., Fischer, P., Brox, T., 2015. U-net: Convolutional networks for biomedical image segmentation. In: International Conference on Medical image computing and computer-assisted intervention. Springer, pp. 234–241.
- Roy, D.P., Huang, H., Boschetti, L., Giglio, L., Yan, L., Zhang, H.H., et al., 2019. Landsat-8 and Sentinel-2 burned area mapping-A combined sensor multi-temporal change detection approach. *Remote Sens. Environ.* 231, 111254.
- Roy, S.K., Mondal, R., Paoletti, M.E., Haut, J.M., Plaza, A., 2021. Morphological convolutional neural networks for hyperspectral image classification. *IEEE J. Selected Top. Appl. Earth Observ. Remote Sens.* 14, 8689–8702.

- Sagan, V., Maimaitijiang, M., Bhadra, S., Maimaitiyiming, M., Brown, D.R., Sidike, P., Fritschi, F.B., 2021. Field-scale crop yield prediction using multi-temporal WorldView-3 and PlanetScope satellite data and deep learning. *ISPRS J. Photogrammetry Remote Sens.* 174, 265–281.
- Schmidt, M., Weickert, J., 2016. Morphological counterparts of linear shift-invariant scale-spaces. *J. Math. Imaging Vis.* 56 (2), 352–366.
- Sellami, A., Tabbone, S., 2022. Deep neural networks-based relevant latent representation learning for hyperspectral image classification. *Pattern Recognit.* 121, 108224.
- Seydi, S.T., Akhoondzadeh, M., Amani, M., Mahdavi, S., 2021a. Wildfire damage assessment over Australia using sentinel-2 imagery and MODIS land cover product within the google earth engine cloud platform. *Remote Sens.* 13, 220.
- Seydi, S.T., Hasanlou, M., Chanussot, J., 2021b. DSMNN-Net: A Deep Siamese Morphological Neural Network Model for Burned Area Mapping Using Multispectral Sentinel-2 and Hyperspectral PRISMA Images. *Remote Sens.* 13, 5138.
- Seydi, S., Rastiveis, H., 2019. A deep learning framework for roads network damage assessment using post-earthquake Lidar data. *Int. Arch. Photogrammetry, Remote Sens. Spatial Inf. Sciences.*
- Shen, Y., Zhong, X., Shih, F.Y., 2019. Deep morphological neural networks. arXiv preprint arXiv:1909.01532.
- Shiraishi, T., Hirata, R., 2021. Estimation of carbon dioxide emissions from the megafires of Australia in 2019–2020. *Sci. Rep.* 11, 1–10.
- Smith-Ramirez, C., Castillo-Mandujano, J., Becerra, P., Sandoval, N., Fuentes, R., Allende, R., et al., 2022. Combining remote sensing and field data to assess recovery of the Chilean Mediterranean vegetation after fire: Effect of time elapsed and burn severity. *Forest Ecol. Manage.* 503, 119800.
- Syifa, M., Panahi, M., Lee, C.-W., 2020. Mapping of post-wildfire burned area using a hybrid algorithm and satellite data: the case of the camp fire wildfire in California, USA. *Remote Sens.* 12, 623.
- Velasco-Forero, S., Pages, R., Angulo, J., 2022. Learnable Empirical Mode Decomposition based on Mathematical Morphology. *SIAM J. Imaging Sci.* 15 (1), 23–44.
- Vetrata, Y., Cochrane, M.A., Priyatna, M., Sukowati, K.A., Khomarudin, M.R., 2021. Evaluating accuracy of four MODIS-derived burned area products for tropical peatland and non-peatland fires. *Environ. Res. Lett.* 16, 035015.
- Wang, D., Guan, D., Zhu, S., Kinnon, M.M., Geng, G., Zhang, Q., Zheng, H., Lei, T., Shao, S., Gong, P., Davis, S.J., 2021. Economic footprint of California wildfires in 2018. *Nature Sustain.* 4 (3), 252–260.
- Wang, J., Sun, K.e., Cheng, T., Jiang, B., Deng, C., Zhao, Y., Liu, D., Mu, Y., Tan, M., Wang, X., Liu, W., Xiao, B., 2021. Deep high-resolution representation learning for visual recognition. *IEEE Trans. Pattern Anal. Mach. Intelligence* 43 (10), 3349–3364.
- Wang, Z., Yang, P., Liang, H., Zheng, G., Yin, J., Tian, Y.e., Cui, W., 2022. Semantic segmentation and analysis on sensitive parameters of forest fire smoke using smoke-unet and landsat-8 imagery. *Remote Sens.* 14 (1), 45.
- Warner, T.A., Skowronski, N.S., Gallagher, M.R., 2017. High spatial resolution burn severity mapping of the New Jersey Pine Barrens with WorldView-3 near-infrared and shortwave infrared imagery. *Int. J. Remote Sens.* 38 (2), 598–616.
- Wu, X., Hong, D., Chanussot, J., 2021. Convolutional neural networks for multimodal remote sensing data classification. *IEEE Trans. Geosci. Remote Sens.* 60, 1–10.
- Xu, W., Wooster, M.J., Polehampton, E., Yemelyanova, R., Zhang, T., 2021b. Sentinel-3 active fire detection and FRP product performance-Impact of scan angle and SLSTR middle infrared channel selection. *Remote Sens. Environ.* 261, 112460.
- Xu, J., Yang, J., Xiong, X., Li, H., Huang, J., Ting, K., et al., 2021a. Towards interpreting multi-temporal deep learning models in crop mapping. *Remote Sens. Environ.* 264, 112599.
- Yu, C., Han, R., Song, M., Liu, C., Chang, C.-I., 2020. A simplified 2D–3D CNN architecture for hyperspectral image classification based on spatial-spectral fusion. *IEEE J. Selected Top. Appl. Earth Observ. Remote Sens.* 13, 2485–2501.
- Zhang, P., Ban, Y., Nascetti, A., 2021b. Learning U-Net without forgetting for near real-time wildfire monitoring by the fusion of SAR and optical time series. *Remote Sens. Environ.* 261, 112467.
- Zhang, Q., Ge, L., Zhang, R., Metternicht, G.I., Du, Z., Kuang, J., et al., 2021c. Deep-learning-based burned area mapping using the synergy of Sentinel-1&2 data. *Remote Sens. Environ.* 264, 112575.
- Zhang, X., Su, H., Zhang, C., Gu, X., Tan, X., Atkinson, P.M., 2021d. Robust unsupervised small area change detection from SAR imagery using deep learning. *ISPRS J. Photogrammetry Remote Sens.* 173, 79–94.
- Zhang, G., Wang, M., Liu, K., 2021a. Deep neural networks for global wildfire susceptibility modelling. *Ecol. Indic.* 127, 107735.
- Zhao, F., Sun, R., Zhong, L., Meng, R., Huang, C., Zeng, X., et al., 2022. Monthly mapping of forest harvesting using dense time series Sentinel-1 SAR imagery and deep learning. *Remote Sens. Environ.* 269, 112822.